

An ALMA search for substructure and fragmentation in starless cores in Orion B North

SAMUEL D. FIELDER ¹, HELEN KIRK ^{2,1}, MICHAEL M. DUNHAM ³ AND STELLA S. R. OFFNER ⁴

¹*Department of Physics and Astronomy, University of Victoria, Victoria, BC, V8P 1A1, Canada*

²*Herzberg Astronomy and Astrophysics Research Centre, National Research Council of Canada, 5071 West Saanich Road, Victoria, BC, V9E 2E7, Canada*

³*Department of Physics, State University of New York at Fredonia, Fredonia, NY 14063, USA*

⁴*Department of Astronomy, The University of Texas at Austin, Austin, TX 78712, USA*

ABSTRACT

We present Atacama Large Millimeter/submillimeter Array (ALMA) Cycle 3 observations of 73 starless and protostellar cores in the Orion B North molecular cloud. We detect a total of 34 continuum sources at 106 GHz, and after comparisons with other data, 4 of these sources appear to be starless. Three of the four sources are located near groupings of protostellar sources, while one source is an isolated detection. We use synthetic observations of a simulation modeling a collapsing turbulent, magnetized core to compute the expected number of starless cores that should be detectable with our ALMA observations and find at least two (1.52) starless core should be detectable, consistent with our data. We run a simple virial analysis of the cores to put the Orion B North observations into context with similar previous ALMA surveys of cores in Chamaeleon I and Ophiuchus. We conclude that the Chamaeleon I starless core population is characteristically less bounded than the other two populations, along with external pressure contributions dominating the binding energy of the cores. These differences may explain why the Chamaeleon I cores do not follow turbulent model predictions, while the Ophiuchus and Orion B North cores are consistent with the model.

1. INTRODUCTION

Dense molecular cloud cores, sub-parsec scale (<0.2 pc) over-densities within molecular clouds, are the immediate progenitors of stars (Bergin & Tafalla 2007; di Francesco et al. 2007). Star formation is an inherently multi-scale process, and we access the wide variety of scales, from cloud to core, by way of different observations. The types of structures present at each scale may provide evidence as to which physical processes are dominant and how they govern star formation. Turbulence is thought to offer global support to the overall molecular cloud collapse, while also driving local collapse at the core scale (Mac Low & Klessen 2004; Ballesteros-Paredes et al. 2007). Studies of the role of turbulence in the transition from dense cores to individual protostars can provide a deeper understanding for hallmark results in the theory of star formation, such as the initial mass function (Goodwin et al. 2008; Holman et al. 2013; Offner et al. 2014), and protostellar multiplicity (Chen et al. 2013; Lomax et al. 2015; Offner et al. 2023).

Around half of all stars exist in binary or multiple systems (Moe & Di Stefano 2017), likely driven by some combination of disk fragmentation, core fragmentation and dynamical capture (see recent review by Offner et al. 2023). Recent observational studies in the Perseus cloud

(Tobin et al. 2016) and the Orion cloud (Tobin et al. 2020) show that there is a distinct bimodal distribution in the separations of multiple stars systems, with peaks at ~ 75 au and ~ 3000 au. Tobin et al. (2020) attribute the larger separation peak to core fragmentation processes, while the smaller peak is attributed to disk fragmentation processes. Additionally, simulations of star formation in turbulent molecular clouds show that a significant fraction of smaller separation multiples can be produced by significant orbital evolution following core fragmentation (Lee et al. 2019; Kuruwita & Haugbølle 2023).

Pokhrel et al. (2018) performed a multi-scale fragmentation study ranging from cloud (≥ 10 pc) to core (~ 10 au), indicating that at all scales, the number of substructures within parent structures was lower than expected from thermal Jeans fragmentation. On the larger scales, observed separations of dense cores along filamentary structures often show inconsistencies with classical analytic cylindrical fragmentation models without the consideration of magnetic fields or turbulence (e.g., André et al. 2014; Könyves et al. 2020). Other studies on fragmentation on smaller scales, those within dense cores, similarly show fewer substructures than expected from a thermal Jeans model (e.g., Das et al.

2021). Meanwhile, studies such as Ohashi et al. (2018) and Palau et al. (2015) show that the separations between substructures within cores are consistent with thermal Jeans lengths. Further studies on fragmentation within dense cores are clearly needed to discern the importance of which physics are at play. The Atacama Large Millimetre/submillimetre Array (ALMA) provides an efficient avenue to search for rare very high-density peaks within starless cores, a natural indicator for thermal versus turbulent processes, where thermal-only processes take longer to form small high-density peaks (Dunham et al. 2016). Population studies, in general, through the total number of detections, can provide a basis to evaluate whether fragmentation within the core is more consistent with thermal or turbulent origins.

Large field-of-view (sub)millimeter observations have proven useful as a way of efficiently mapping entire star forming regions and their dense core populations. These dust continuum studies are good tracers of column density peaks, and can therefore characterize the locations, sizes and approximate masses of entire dense core populations (e.g., Motte et al. 1998; Enoch et al. 2007; Ward-Thompson et al. 2007; Könyves et al. 2015). Early (sub)millimetre studies indicated that starless cores have inner flat density substructures (Ward-Thompson et al. 1994), and that the density profiles are often approximated as smooth Bonnor-Ebert (BE) spheres, which are centrally flat, and roughly drop as r^{-2} toward the edge (Ebert 1955; Bonnor 1956). However, these single-dish (sub)millimetre observations lack the sufficient angular resolution to probe the inner structures where fragmentation could be taking place.

High resolution facilities, like interferometers, are needed to be able to resolve the structure present within dense cores, leading to a more complete look at the role of core fragmentation. The earliest large interferometric survey of starless dense cores was a CARMA (Combined Array for Research in Millimetre-wave Astronomy) survey of 12 dense cores in the Perseus molecular cloud (Schnee et al. 2010). Despite observing each core for 8 hours, no detectable substructure was found (Schnee et al. 2010). Offner et al. (2012) showed that CARMA most likely lacked the sensitivity needed to detect substructure, and that ALMA would have the necessary sensitivity to see core substructure resulting from turbulence-driven fragmentation.

Interferometers by nature are only sensitive to a range of angular scales, the values of which are set by the observed wavelength and separations between antennas. Highly dense and compact features are best detected with larger antenna separations, with accompanying

poorer sensitivity to larger-scale features. Conversely, more compact antenna configurations, like those observed with ALMA’s Atacama Compact Array (ACA), are much more successful at detecting larger and less dense starless core fragments (e.g., Dutta et al. 2020; Tokuda et al. 2020; Sahu et al. 2021, 2023). In cases that do not have additional larger separation data (e.g., ALMA 12m array data), there is insufficient resolution to determine whether or not there are any compact peaks within the fragments.

The first dense core population study with the ALMA 12m array, to hunt for these rare very high density substructures, was performed by Dunham et al. (2016) in the Chamaeleon I region, however, no substructures were detected for any of the 56 starless cores observed. This contradicts the expected number of detections predicted by synthetic observations generated from simulations turbulent prestellar cores. Dunham et al. (2016) also demonstrated that structures generated from turbulent fragmentation should be detected at a rate approximately 100 times higher than BE sphere modeled cores, for their specific ALMA observations. The factor of 100 less in detectability in BE spheres does not mean they could never be detected: Caselli et al. (2019), for example, demonstrate that an evolved BE sphere model fit to the highly evolved starless core L1544 would have a central flat region only $1.75''$ (~ 250 au at a distance of 140 pc) with their ALMA 12m plus ACA observations, making a detection likely. The main difference between turbulently collapsing cores and non-turbulent, smoothly collapsing cores is the lifetime of the high-density peaks, with collapse occurring earlier in the case with turbulence (Offner et al. 2012).

Following the Chamaeleon I ALMA study, Kirk et al. (2017a) performed a population study of the L1688 molecular cloud in Ophiuchus, where the predictions derived from synthetic observations of the same turbulent fragmentation simulations matched the observed two compact substructure detections.

To date, several other groups have carried out deeper observations, including the use of the ACA, to provide better sensitivity to larger-scale features (e.g., Sato et al. 2023; Hirano et al. 2024). Tokuda et al. (2020) performed observations with the ACA of 39 dense cores (32 starless and 7 protostellar) in the Taurus molecular cloud, achieving an angular resolution of $6.5''$ (~ 900 au). Tokuda et al. (2020) detected multiple complex substructures with a typical size scale of ~ 1000 au across a total of 12 of the observed starless cores. Additionally, Sahu et al. (2021), through the ALMA Survey of Orion Planck Galactic Cold Clumps (ALMASOP), have performed detailed studies on the substructure of five

dense cores, probing much higher resolution scales down to $0.8''$ (~ 320 au). One core studied showed clear signatures of fragmentation, characterized by relatively high density ($2 - 8 \times 10^7 \text{ cm}^{-3}$) and separations of ~ 1200 au (Sahu et al. 2021), including one instance of a proto-quadruple system (Luo et al. 2023). Although the results of both Tokuda et al. (2020) and Sahu et al. (2021) indicate potential agreement with the turbulent fragmentation model, both studies do not explicitly test the number of starless core detections.

To complement the previous studies performed by Dunham et al. (2016) and Kirk et al. (2017a), we present results from a similarly designed survey of starless cores in the Orion B molecular cloud. In contrast to Chamaeleon I and Ophiuchus, Orion is the closest high-mass star-forming region, with the Orion B North portion of the complex situated at a distance of approximately 419 pc (Zucker et al. 2019). As noted earlier, the number of detections of high density peaks in Dunham et al. (2016) and Kirk et al. (2017a) taken together were puzzling, with Dunham et al. (2016) showing a strong disagreement with the predictions from the turbulent simulations, while Kirk et al. (2017a) agreed well. One possible explanation for this discrepancy is the dynamical state of the population of dense cores in each cloud; indeed, Tsitali et al. (2015) showed that most dense cores in Chamaeleon I appear unbound, indicating that the cores may be dispersing rather than evolving to form stars. Utilizing comparable datasets for all three regions, we analyze the boundedness of the dense core populations, and use these results to interpret the number of detections of high density peaks within Orion B North in the broader context.

In this paper, we present an ALMA 3 mm continuum survey of 73 dense cores in the Orion B North molecular cloud. In Section 2, we present the observations and data reduction applied, and in Section 3, we perform a catalog search for any associated protostellar sources. In Section 4 we analyze the ALMA detections and estimate their radius, mass and number density. In Section 5, we use numerical simulations of starless core evolution to create synthetic observations to predict the expected number of starless core detections in our dataset. In Section 6, we consider our results in the context of the previous ALMA population studies, and run a simple virial analysis to explore whether differences in core boundedness is a plausible explanation for the varied levels of agreement from the turbulent fragmentation model. We summarize our findings in Section 7.

2. OBSERVATIONS

2.1. Target Selection: SCUBA

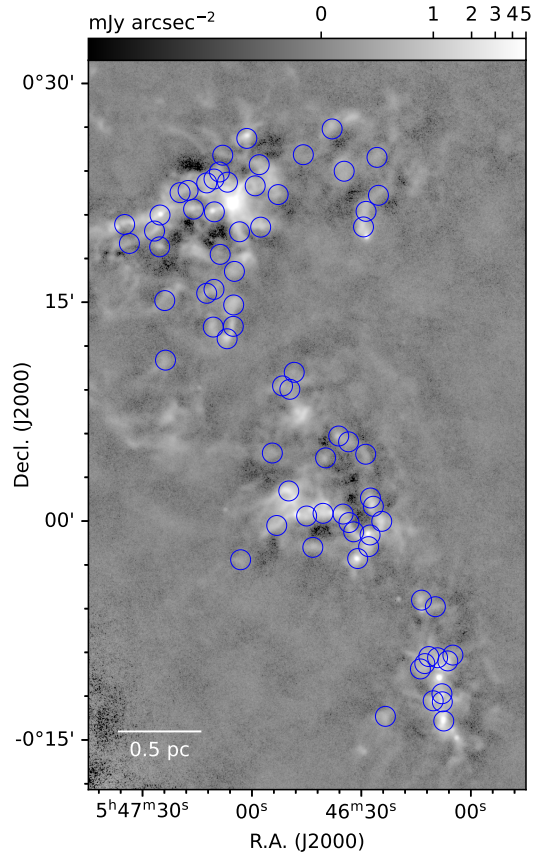


Figure 1. SCUBA2 $850 \mu\text{m}$ image of the Orion BN cloud adapted from Kirk et al. (2016). The blue circles show all 73 starless dense cores identified by NWT07 which were observed by ALMA, with the diameters of the circles equal to the primary beam of the 12 m observations.

In their re-analysis of all SCUBA archive data of the Orion star-forming regions, Nutter & Ward-Thompson (2007) (hereafter NWT07) identified a total of 393 dense cores in the Orion molecular cloud complex. The detected cores were classified as protostellar or starless using archival data from the Spitzer Space Telescope. In the Orion B North portion of the complex, covering the area of NGC 2068/2071, 73 of the 100 dense cores were classified as starless (NWT07). The NWT07 catalog is sensitive down to a mass of $0.1M_{\odot}$ and maps the entirety of the NGC 2068/2071 star forming regions. We obtained ALMA Cycle 3 observations of all 73 starless cores identified by NWT07 in the Orion B North region. Figure 1 shows the 73 ALMA pointings overlaid on a more recent SCUBA-2 $850 \mu\text{m}$ image of Orion BN presented by Kirk et al. (2016), and positional information is given in Table 1.

2.2. ALMA Data

The ALMA Band 3 data were observed between 2016 March 08 and 2016 August 27, and consisted of 7 unique observation times, using an average of 38 antennas. Four spectral windows were used, with three configured for continuum measurements, centered at 101 GHz, 103 GHz, and 113 GHz, each with a bandwidth of 1875 MHz. The total continuum bandwidth is therefore approximately 6 GHz at a central frequency of 106 GHz. The last spectral window was configured for observation of ^{12}CO (1 – 0) emission at 115 GHz. Our main focus in this study is the continuum data; we use the CO line data appropriately when needed (see Section 3.2 for details).

Flux and bandpass calibrators were observed at the beginning of each execution block, followed by single pointings of all 73 science targets, with periodic phase gain calibrators therein. Most sources (50) were observed during all 7 execution blocks, totalling 270 seconds of on source time, with the remaining (23) sources missing the last execution block, totalling 230 seconds of on-source time. These continuum observations were requested to have a 1σ rms noise of $0.07 \text{ mJy beam}^{-1}$, and was achieved for all ALMA pointings (see Table 1 and below for details).

The array was in a relatively compact configuration for the first five observation windows (C-2/3), with antenna separations ranging from approximately 15 m to 460 m. In the final two observations, the array was in a slightly more expanded configuration (C-4/5) with antenna separations ranging from approximately 15 m to 1125 m. This yields an average synthesized beam of $1.5'' \times 1.3'' (\sim 630 \text{ au} \times 550 \text{ au})$ at a position angle of 75 degrees, along with a maximum recoverable scale of approximately $14''$. There is no significant difference in the synthesized beam between sources that were only observed for 230 seconds, and those observed for the full 270 seconds.

The calibration and reduction was conducted in the pipeline version 4.7.0 of the Common Astronomy Soft-

ware Applications (CASA) software. For imaging and analysis, CASA version 6.5.0 was utilized for its refined automasking routines (The CASA Team et al. 2022).

To construct the continuum images, the line emission was first subtracted from the last spectral window in order to make use of all available continuum emission present, along with these standard choices of imaging parameters: Briggs weighting with a robust value of $R = 0.5$, a uvtaper of $0.8''$ to reduce side-lobe contamination, and default automasking parameters. Self-calibration routines were performed on the continuum where it improved image quality, which in our case was where the peak emission was above approximately 10 mJy beam^{-1} . This brought all fields to the rms noise level requested for the observations, $0.07 \text{ mJy beam}^{-1}$. In the case where the field of view of individual ALMA observations overlapped, mosaicking was conducted (prior to self-calibration where appropriate) to improve the final sensitivity of the image. The observations lying within a mosaicked area are noted in Table 1.

For line emission imaging, the continuum was first subtracted, along with only one change with respect to the above parameters, a modified version of the Briggs weighting scheme called `briggsbwtaper`, with the same robust value of $R = 0.5$. The purpose with this choice of weighting scheme is to modify the cube imaging weights to have a similar density to that of the continuum imaging weights (The CASA Team et al. 2022), which gave the best results in our images. We use this data as an indicator for protostellar nature, as the data achieves a sensitivity of 1.1 K in a 0.5 km s^{-1} channel, which is sufficient to detect outflow signatures, if any are present near our identified detections.

All final images produced were corrected for primary beam attenuation. We subsequently use CASA’s `imfit` task to fit elliptical Gaussians to all continuum sources found.

Table 1. Noise Levels of Targeted ALMA Observations

Field ^a	R.A.	Decl.	ALMA Mosaic Field ^b	1σ rms ^c	Int. Time ^d	YSO ^e
	(J2000)	(J2000)		(mJy beam ⁻¹)	(s)	
BN-546049-00911	05:46:04.90	-00:09:11.00	BN-546049-00911Mosaic	0.045	270	N
BN-546063-00935	05:46:06.30	-00:09:35.00	BN-546049-00911Mosaic	0.045	270	Y
BN-546074-01342	05:46:07.40	-00:13:42.00	BN-546074-01342Mosaic	0.061	270	Y
BN-546078-01223	05:46:07.80	-00:12:23.00	BN-546074-01342Mosaic	0.061	270	Y

Table 1 continued

Table 1 (continued)

Field ^a	R.A.	Decl.	ALMA Mosaic Field ^b	1 σ rms ^c	Int. Time ^d	YSO ^e
	(J2000)	(J2000)		(mJy beam ⁻¹)	(s)	
BN-546079-01150	05:46:07.90	-00:11:50.00	BN-546074-01342Mosaic	0.061	270	Y
BN-546091-00922	05:46:09.10	-00:09:22.00	BN-546049-00911Mosaic	0.045	270	N
BN-546097-00552	05:46:09.70	-00:05:52.00	BN-546097-00552Mosaic	0.054	270	N
BN-546103-01219	05:46:10.30	-00:12:19.00	BN-546074-01342Mosaic	0.061	270	Y
BN-546115-00917	05:46:11.50	-00:09:17.00	BN-546049-00911Mosaic	0.045	270	N
BN-546126-00946	05:46:12.60	-00:09:46.00	BN-546049-00911Mosaic	0.045	270	N
BN-546135-00525	05:46:13.50	-00:05:25.00	BN-546097-00552Mosaic	0.054	270	Y
BN-546138-01008	05:46:13.80	-00:10:08.00	BN-546049-00911Mosaic	0.045	270	N
BN-546234-01323	05:46:23.40	-00:13:23.00	...	0.050	270	N
BN-546244-00001	05:46:24.40	-00:00:01.00	BN-546244-00001Mosaic	0.054	270	N
BN-546253+02220	05:46:25.30	+00:22:20.00	...	0.053	230	N
BN-546257+02456	05:46:25.70	+00:24:56.00	...	0.057	230	N
BN-546267+00101	05:46:26.70	+00:01:01.00	BN-546244-00001Mosaic	0.054	270	N
BN-546275+00135	05:46:27.50	+00:01:35.00	BN-546244-00001Mosaic	0.054	270	N
BN-546276-00057	05:46:27.60	-00:00:57.00	BN-546244-00001Mosaic	0.076*	270	Y
BN-546280-00145	05:46:28.00	-00:01:45.00	BN-546244-00001Mosaic	0.054	270	N
BN-546287+02114	05:46:28.70	+00:21:14.00	BN-546287+02114Mosaic	0.055	230	N
BN-546288+00435	05:46:28.80	+00:04:35.00	...	0.047	270	N
BN-546294+02010	05:46:29.40	+00:20:10.00	BN-546287+02114Mosaic	0.055	230	N
BN-546310-00234	05:46:31.00	-00:02:34.00	BN-546244-00001Mosaic	0.054	270	Y
BN-546321-00044	05:46:32.10	-00:00:44.00	BN-546244-00001Mosaic	0.054	270	N
BN-546334-00006	05:46:33.40	-00:00:06.00	BN-546244-00001Mosaic	0.054	270	Y
BN-546335+00526	05:46:33.50	+00:05:26.00	BN-546335+00526Mosaic	0.047	270	N
BN-546347+02359	05:46:34.70	+00:23:59.00	...	0.056	230	N
BN-546350+00029	05:46:35.00	+00:00:29.00	BN-546244-00001Mosaic	0.054	270	N
BN-546362+00550	05:46:36.20	+00:05:50.00	BN-546335+00526Mosaic	0.047	270	N
BN-546380+02653	05:46:38.00	+00:26:53.00	...	0.060	230	N
BN-546398+00420	05:46:39.80	+00:04:20.00	...	0.048	270	Y
BN-546405+00032	05:46:40.50	+00:00:32.00	BN-546405+00032Mosaic	0.050	270	N
BN-546433-00148	05:46:43.30	-00:01:48.00	...	0.054	270	N
BN-546450+00021	05:46:45.00	+00:00:21.00	BN-546405+00032Mosaic	0.050	270	N
BN-546459+02507	05:46:45.90	+00:25:07.00	...	0.059	230	N
BN-546484+01012	05:46:48.40	+00:10:12.00	BN-546484+01012Mosaic	0.042	270	N
BN-546496+00902	05:46:49.60	+00:09:02.00	BN-546484+01012Mosaic	0.042	270	N
BN-546499+00204	05:46:49.90	+00:02:04.00	...	0.049	270	N
BN-546516+00916	05:46:51.60	+00:09:16.00	BN-546484+01012Mosaic	0.042	270	N
BN-546528+02223	05:46:52.80	+00:22:23.00	...	0.054	230	N
BN-546532-00018	05:46:53.20	-00:00:18.00	...	0.051	270	N
BN-546544+00440	05:46:54.40	+00:04:40.00	...	0.047	270	N
BN-546576+02009	05:46:57.60	+00:20:09.00	...	0.054	230	N

Table 1 continued

Table 1 (continued)

Field ^a	R.A.	Decl.	ALMA Mosaic Field ^b	1 σ rms ^c	Int. Time ^d	YSO ^e
	(J2000)	(J2000)		(mJy beam ⁻¹)	(s)	
BN-546580+02426	05:46:58.00	+00:24:26.00	...	0.058	230	N
BN-546591+02259	05:46:59.10	+00:22:59.00	...	0.055	230	N
BN-547014+02614	05:47:01.40	+00:26:14.00	...	0.059	230	Y
BN-547031-00239	05:47:03.10	-00:02:39.00	...	0.053	270	N
BN-547034+01950	05:47:03.40	+00:19:50.00	...	0.054	270	N
BN-547048+01707	05:47:04.80	+00:17:07.00	...	0.050	270	N
BN-547050+01449	05:47:05.00	+00:14:49.00	...	0.049	270	N
BN-547051+01321	05:47:05.10	+00:13:21.00	BN-547051+01321Mosaic	0.050	270	N
BN-547067+02314	05:47:06.70	+00:23:14.00	BN-547067+02314Mosaic	0.049	230	N
BN-547068+01230	05:47:06.80	+00:12:30.00	BN-547051+01321Mosaic	0.050	270	N
BN-547080+02505	05:47:08.00	+00:25:05.00	BN-547067+02314Mosaic	0.049	230	N
BN-547087+01817	05:47:08.70	+00:18:17.00	...	0.052	270	N
BN-547089+02356	05:47:08.90	+00:23:56.00	BN-547067+02314Mosaic	0.049	230	N
BN-547103+02112	05:47:10.30	+00:21:12.00	...	0.066	230	Y
BN-547104+01553	05:47:10.40	+00:15:53.00	BN-547104+01553Mosaic	0.045	270	N
BN-547104+02327	05:47:10.40	+00:23:27.00	BN-547067+02314Mosaic	0.049	230	Y
BN-547106+01318	05:47:10.60	+00:13:18.00	BN-547051+01321Mosaic	0.050	270	N
BN-547124+01537	05:47:12.40	+00:15:37.00	BN-547104+01553Mosaic	0.045	270	N
BN-547124+02311	05:47:12.40	+00:23:11.00	BN-547067+02314Mosaic	0.049	230	N
BN-547160+02123	05:47:16.00	+00:21:23.00	BN-547160+02123Mosaic	0.048	230	Y
BN-547175+02240	05:47:17.50	+00:22:40.00	BN-547160+02123Mosaic	0.048	230	N
BN-547197+02231	05:47:19.70	+00:22:31.00	BN-547160+02123Mosaic	0.048	230	N
BN-547237+01102	05:47:23.70	+00:11:02.00	...	0.048	270	N
BN-547239+01507	05:47:23.90	+00:15:07.00	...	0.051	270	N
BN-547252+02059	05:47:25.20	+00:20:59.00	BN-547252+02059Mosaic	0.055	230	Y
BN-547253+01848	05:47:25.30	+00:18:48.00	BN-547252+02059Mosaic	0.055	270	N
BN-547267+01953	05:47:26.70	+00:19:53.00	BN-547252+02059Mosaic	0.055	230	N
BN-547336+01902	05:47:33.60	+00:19:02.00	BN-547336+01902Mosaic	0.054	270	N
BN-547349+02020	05:47:34.90	+00:20:20.00	BN-547336+01902Mosaic	0.054	230	N

^aObserved SCUBA core name from [Nutter & Ward-Thompson \(2007\)](#).

^bFor individual fields which overlap in coverage, the mosaic field name is given (taken to be the eastern-most field).

^c1 σ root-mean-square noise, computed in non-detection areas of the (mosaicked, if applicable) field. This value was computed from the non-primary beam corrected image.

^dTotal integration time on the individual field.

^eProtostellar classification based on more recent catalogs studied (see Section 3.1 for details).

*Due to a bright central protostellar source, we report a more representative value of rms for this individual field, as opposed to the rms value computed for the mosaicked field.

Table 2. Observed Properties of ALMA Detections

Src	R.A.	Decl.	Pk ^a	Pk _{err} ^a	Tot ^a	Tot _{err} ^a	FWHM _a ^a	FWHM _b ^a	P.A. ^a	FWHM _{a,d} ^b	FWHM _{b,d} ^b	P.A. ^a	P.A. ^b		
#	(J2000)	(J2000)	(mJy beam ⁻¹)	(mJy)	(mJy)	(mJy)	(arcsec)	(arcsec)	(deg)	(arcsec)	(arcsec)	(deg)	(deg)		
										fit	err	fit	err		
1	05:46:06.01	-00:09:32.70	0.36	0.08	4.60	1.03	5.47	4.62	59	5.26	1.22	4.43	1.07	58	53
2	05:46:07.26	-00:13:30.27	9.48	0.16	12.22	0.33	1.85	1.51	71	0.84	0.09	0.74	0.08	65	66
3	05:46:07.33	-00:13:43.49	31.37	0.16	36.88	0.31	1.78	1.43	70	0.68	0.03	0.56	0.03	57	12
4	05:46:07.51	-00:13:54.79	0.45	0.16	1.36	0.63	2.98	2.18	162	2.67	1.19	1.42	1.04	162	42
5	05:46:07.53	-00:11:49.22	0.97	0.14	5.25	0.90	4.34	2.69	152	4.14	0.74	2.14	0.49	153	11
6	05:46:07.73	-00:12:21.27	14.37	0.17	21.73	0.38	1.98	1.66	83	1.15	0.06	0.94	0.06	110	12
7	05:46:07.84	-00:09:59.61	6.45	0.11	7.59	0.21	1.73	1.36	65	0.81	0.07	0.36	0.10	62	8
8	05:46:07.86	-00:10:01.33	2.74	0.11	3.44	0.23	1.75	1.43	63	0.88	0.17	0.56	0.23	57	48
9	05:46:08.42	-00:10:01.03	0.86	0.09	5.53	0.69	4.75	2.70	39	4.52	0.60	2.33	0.34	38	8
10	05:46:08.49	-00:10:03.10	8.13	0.10	7.55	0.17	1.44	1.28	83	-1.00	-1.00	-1.00	-1.00	-1	-1
11	05:46:08.92	-00:09:56.11	2.07	0.11	2.28	0.20	1.58	1.39	74	0.51	0.31	0.36	0.21	129	73
12	05:46:10.04	-00:12:16.83	39.04	0.15	40.36	0.28	1.66	1.35	72	0.31	0.03	0.19	0.09	165	24
13	05:46:13.13	-00:06:04.94	9.41	0.14	11.18	0.27	1.66	1.38	67	0.71	0.07	0.50	0.08	60	19
14	05:46:14.20	-00:05:26.71	0.51	0.13	0.54	0.24	1.70	1.18	80	-1.00	-1.00	-1.00	-1.00	-1	-1
15	05:46:27.91	-00:00:52.11	65.62	0.14	73.72	0.27	1.66	1.41	74	0.52	0.02	0.49	0.02	43	26
16	05:46:28.34	+00:19:49.18	1.47	0.14	1.79	0.28	1.82	1.39	78	0.93	0.36	0.42	0.27	77	82
17	05:46:28.61	+00:20:58.08	0.50	0.13	0.49	0.23	1.68	1.21	127	-1.00	1.59	-1.00	0.60	-1	-1
18	05:46:30.91	-00:02:35.07	7.55	0.15	17.54	0.47	2.46	1.97	64	1.89	0.07	1.45	0.06	58	7
19	05:46:31.09	-00:02:32.95	16.15	0.15	25.05	0.35	1.86	1.74	152	1.31	0.03	0.73	0.05	160	5
20	05:46:43.12	+00:00:52.47	1.70	0.13	2.40	0.28	1.76	1.62	2	1.15	0.33	0.56	0.42	169	36
21	05:46:46.52	+00:00:16.09	1.00	0.12	1.04	0.22	1.53	1.37	64	-1.00	1.05	-1.00	0.50	-1	-1
22	05:46:47.03	+00:00:27.20	1.96	0.13	3.55	0.34	2.21	1.65	110	1.69	0.25	0.83	0.30	118	13
23	05:46:47.43	+00:00:23.24	1.10	0.09	12.48	1.10	5.31	4.32	38	5.11	0.47	4.09	0.39	36	22
24	05:46:47.51	+00:00:29.50	0.85	0.10	7.75	1.04	5.55	3.32	10	5.38	0.75	2.97	0.45	9	9
25	05:46:47.69	+00:00:25.02	5.38	0.13	7.22	0.27	1.81	1.50	54	1.01	0.11	0.64	0.13	37	15
26	05:46:47.97	+00:01:41.80	1.10	0.13	2.55	0.42	2.67	1.68	38	2.24	0.48	0.99	0.43	34	15
27	05:46:57.30	+00:23:57.94	3.39	0.16	4.25	0.33	1.67	1.42	72	0.83	0.21	0.55	0.34	61	72

Table 2 continued

Table 2 (continued)

Src #	R.A. (J2000)	Decl. (J2000)	Pk ^a (mJy beam ⁻¹)	Pk _{err} ^a	Tot ^a (mJy)	Tot _{err} ^a	FWHM _a ^a (arcsec)	FWHM _b ^a (arcsec)	P.A. ^a (deg)	FWHM _{a,d} ^b (arcsec)	FWHM _{b,d} ^b (arcsec)	P.A.-d (deg)	
										fit	err	fit	err
28	05:47:00.92	+00:26:21.98	2.65	0.16	9.34	0.71	2.78	2.36	161	2.46	0.21	1.87	0.19
29	05:47:01.31	+00:26:23.09	4.91	0.17	6.96	0.37	1.78	1.48	93	1.05	0.12	0.72	0.13
30	05:47:10.61	+00:21:13.78	12.17	0.16	16.31	0.35	1.75	1.49	84	0.93	0.06	0.70	0.06
31	05:47:15.95	+00:21:22.89	2.02	0.13	2.70	0.28	1.80	1.55	89	0.92	0.29	0.75	0.51
32	05:47:24.84	+00:20:58.98	16.42	0.15	51.09	0.60	2.77	2.40	134	2.39	0.04	1.84	0.04
33	05:47:32.45	+00:20:21.60	5.56	0.15	7.19	0.30	1.74	1.50	99	0.91	0.14	0.60	0.20
34	05:47:36.56	+00:20:05.89	8.36	0.15	10.28	0.29	1.65	1.51	79	0.75	0.07	0.58	0.12

^aProperties of the Gaussian fit to the ALMA emission: peak flux, integrated flux, major and minor axes of the FWHM, and position angle of the FWHM.

^bProperties of the deconvolved Gaussian fit: major and minor axes of the FWHM, and position angle of the FWHM. Unresolved sources are indicated by values of -1.

3. DETECTIONS

We detect a total of 34 continuum sources across 19 individual ALMA pointings. Table 2 lists each of the continuum sources with a running index number, location information based on the center of the two-dimensional Gaussian fit and additional associated statistics. These include the peak emission, the total flux, the major and minor axes, as well as the position angle. We also show the deconvolved values (and their uncertainties) for the size, and positional angle; with a -1 indicator if partially or fully unresolved.

3.1. Protostellar Associations

As introduced in Section 2.1, NWT07 identified 73 starless core candidates in their re-analysis of all SCUBA archival data in the Orion B North region. Since this time, there have been many studies of protostellar sources in the Orion molecular cloud complex, which have revealed many previously unknown protostars. Our observations will easily detect protostellar sources, and due to the statistical nature of our analysis, an accurate measure of the starless core population is needed. We have examined a number of different catalogs to check for any protostellar sources, which can be associated with our 34 ALMA detections. Table 3 lists each of our 34 ALMA detections along with each nearest protostellar source in all of the catalogs studied.

In summary, all but five of our ALMA detections are directly associated with a protostellar source, with one of those showing signs of a protostellar outflow in the CO data (see Section 3.2 for details). The results from our protostellar catalog searches, as they pertain to the 34 ALMA detections are detailed in the following sections.

We perform an analogous check for the original starless core population identified by NWT07 for use in our statistical analysis (see Section 3.3 for details).

3.1.1. Associations with Spitzer YSOs

We first search for the nearest Spitzer YSO in the Megeath et al. (2012) catalog. The separations found with this catalog fall into two main domains, those with very small separations ($<2''$), and those with larger separations ($>13''$). There are three such detections which lie in moderate separation range, source 23, 24, and 27, with a separation of $4.5''$, $5.3''$, and $7.8''$ to the nearest Spitzer YSO, respectively. Of these three Spitzer YSOs, the two nearest ALMA sources 23 and 24 are already more directly associated with other ALMA detections. The additional catalogues examined later in this section provided clarity on the protostellar/starless classification for these three detections.

In this study, we classify separations of less than $2''$ to the nearest Spitzer YSO to be coincident detections. In

total, we find that 27 of our ALMA detections are found in the Spitzer catalog and we subsequently classify these detections as protostellar in nature.

3.1.2. Associations with ALMA-based Catalogs

We compared our detections to those found in Tobin et al. (2020), The VLA/ALMA Nascent Disk and Multiplicity (VANDAM) Survey of Orion Protostars. This survey population was drawn from the Herschel Orion Protostellar Survey (HOPS) (specifically Fischer et al. 2010; Stutz et al. 2013; Furlan et al. 2016), where all Class 0, Class 1 and Flat Spectrum protostars (with additional constraints) were selected for observations with ALMA Band 7 (0.87 mm), at a resolution of $0.1''$ (40 au), and with the VLA at 9 mm at a resolution of $0.08''$ (32 au). The VANDAM study observed a total of 328 protostars with ALMA, and only 148 protostars with the VLA (Tobin et al. 2020), so we choose to perform our association verification with the published ALMA catalog. Additional visual checks with both catalogs were conducted to ensure that associations in the Orion B North region were not missed. Compared to our ALMA data, the VANDAM observations have a higher angular resolution and reduced ability to recover flux on larger angular scales, hence VANDAM is expected to only detect protostellar sources.

Five ALMA detections do not lie within areas observed with VANDAM, and as such have no associations listed in the catalog. Of the 27 detections lying within VANDAM coverage, 25 have direct correspondences with VANDAM protostars, each with a separation of less than $0.50''$. The remaining two detections, source 23 and 24, lie within the area observed by VANDAM, but no protostellar emission is seen by VANDAM and therefore should be starless.

Additionally, we compare our detections to the 19 sources analyzed by Dutta et al. (2020) in the Orion B region, through the ALMA Survey of Orion Planck Galactic Cold Clumps (ALMASOP). These are ALMA Band 6 (1.3 mm) observations, with a resolution of $0.35''$ (140 au). Due to the ALMASOP survey work covering the entire Orion complex, only nine of our detections are found in the ALMASOP survey, with separations less than approximately $0.5''$, eight of which are classified as protostellar. These same eight sources are also identified as protostars by the VANDAM survey (Tobin et al. 2020). The one remaining ALMASOP associated detection, G205.46-14.56M3, is classified as starless by ALMASOP, in agreement with our final classification of source 1.

Table 3. ALMA Detections and Nearest Catalog Objects

Src	Spitzer (1)	VANDAM (2)	VISTA (3)	SESNA (4)	WISE (5)	HGBS (6)	APEX (7)	ALMASOP (8)
#	Name (")	Name (")	Name (")	Name (")	Name (")	Name (")	Name (")	Name (")
1	3170	HOPS-387-A	40.3	J054607.76-000937.7	26.9	J054607.86-001000.8	43.0	G205.46-14.56M2
2	3161	HOPS-358-A	7.2	J054607.26-001330.0	0.3	J054604.78-001416.6	3.6	G205.46-14.56S1
3	3161	HOPS-358-B	20.5	J054607.26-001330.0	13.5	J054604.78-001416.6	9.9	G205.46-14.56S1
4	3161	HOPS-358-B	32.0	J054607.26-001330.0	25.1	J054604.78-001416.6	21.5	G205.46-14.56S1
5	3166	HOPS-401	9.2	J054607.88-001156.9	9.3	J054607.86-001000.8	5.8	G205.46-14.56N2
6	3163	HOPS-401	24.6	J054607.88-001156.9	24.5	J054604.78-001416.6	26.6	G205.46-14.56N2
7	3168	HOPS-387-A	2.1	J054607.85-001001.1	1.5	J054607.86-001000.8	4.8	G205.46-14.56M2
8	3168	HOPS-387-B	0.4	J054607.85-001001.1	0.2	J054607.86-001000.8	4.5	G205.46-14.56M2
9	3167	HOPS-386-B	8.5	J054608.47-001002.9	2.0	J054607.86-001000.8	4.1	G205.46-14.56M2
10	3167	HOPS-386-A	9.6	J054608.47-001002.9	0.4	J054607.86-001000.8	5.5	G205.46-14.56M2
11	3169	HOPS-386-C	17.0	J054608.94-000956.0	0.2	J054607.86-001000.8	12.7	G205.46-14.56M2
12	3163	HOPS-402	0.0	J054607.88-001156.9	37.9	J054607.86-001000.8	1.5	G205.46-14.56N1
13	3180	HOPS-388	32.2	J054613.14-000604.8	0.2	J054613.13-000604.8	2.0	G205.46-14.56M2
14	3183	HOPS-320	0.5	J054614.22-000526.5	0.3	J054613.13-000604.8	10.9	G205.46-14.56M2
15	3195	HOPS-403	95.5	J054629.55-000135.1	49.5	J054618.50-000017.8	1.8	G205.46-14.56M2
16	3338	HOPS-331	200.6	J054628.34+001949.3	0.2	J054633.31+002255.5	21.4	G205.46-14.56M2
17	3354	HOPS-331	136.9	J054628.59+002058.1	0.2	J054633.31+002255.5	90.4	G205.46-14.56M2
18	3195	HOPS-373-B	4.2	J054629.55-000135.1	63.4	J054618.50-000017.8	0.8	G205.46-14.56M2
19	3195	HOPS-373-A	7.1	J054629.55-000135.1	62.3	J054618.50-000017.8	3.8	G205.46-14.56M2
20	3208	HOPS-363-A	63.5	J054643.11+000052.3	0.3	J054643.12+000052.2	5.5	G205.46-14.56M2
21	3199	HOPS-322	13.4	J054646.51+000016.0	0.2	J054643.12+000052.2	15.7	G205.46-14.56M2
22	3202	HOPS-389-A	0.0	J054647.01+000026.9	0.2	J054643.12+000052.2	4.7	G205.46-14.56M2
23	3201	HOPS-323-B	7.3	J054647.69+000025.2	4.5	J054643.12+000052.2	3.2	G205.46-14.56M2
24	3201	HOPS-323-A	7.9	J054647.69+000025.2	5.0	J054643.12+000052.2	4.6	G205.46-14.56M2
25	3201	HOPS-323-A	10.3	J054647.69+000025.2	0.2	J054643.12+000052.2	5.6	G205.46-14.56M2
26	3215	HOPS-389-B	76.0	J054647.96+000141.8	0.2	J054643.12+000052.2	321.9	G205.46-14.56M2
27	3398	HOPS-338-B	40.6	J054657.35+002350.4	7.6	J054703.69+002328.8	2.0	G205.46-14.56M2
28	3409	HOPS-341	38.3	J054701.07+002544.1	38.0	J054703.69+002328.8	155.7	G205.46-14.56M2
29	3408	HOPS-340	39.5	J054701.07+002544.1	39.2	J054703.69+002328.8	159.0	G205.46-14.56M2
30	3359	HOPS-365	1.8	J054710.62+002113.8	0.1	J054710.61+002114.0	1.5	G205.46-14.56M2
31	3361	HOPS-347	16.3	J054714.89+002118.8	16.3	J054712.90+002206.6	1.6	G205.46-14.56M2
32	3356	HOPS-359	29.0	J054722.90+002058.0	29.1	J054727.74+002035.8	1.4	G205.46-14.56M2
33	3344	HOPS-390	11.5	J054732.44+002021.7	0.2	J054736.60+002005.9	1.5	G205.46-14.56M2
34	3341	HOPS-364-B	74.5	J054736.57+002006.0	0.3	J054736.60+002005.9	5.2	G205.46-14.56M2

Table 3 continued

Table 3 (*continued*)

Src	Spitzer (1)	VANDAM (2)	VISTA (3)	SESNA (4)	WISE (5)	HGBS (6)	APEX (7)	ALMASOP (8)
#	Name	Name	Name	Name	Name	Name	Name	Name
	(")	(")	(")	(")	(")	(")	(")	(")

NOTE—Catalog entry name and separation distance to each of the protostellar catalogs entries, to each of the ALMA detections.

References—(1) Megeath2012; (2) Tobin2020; (3) Spezzi2015; (4) R. Gutermuth 2024, in preparation; (5) Marton2016; (6) Konyves2020; (7) Stutz2013; (8) Dutta2020

3.1.3. Other Published Catalogs

The following catalogs were also parsed for potential protostellar matches: the Herschel Gould Belt Survey (Könyves et al. 2020), the aforementioned Herschel Orion Protostellar Survey (HOPS) (Stutz et al. 2013; Furlan et al. 2016), the VISTA Orion Mini-Survey (Spezzi et al. 2015), the Spitzer Extended Solar Neighborhood Archive (SESNA) (Pokhrel et al. 2020, R. Gutermuth et al. 2024, in preparation) and the Wide-field Infrared Survey Explorer (WISE) all-sky catalog (Marton et al. 2016). No new protostellar candidates were identified based on these catalogues, but the associations that we find are included in Table 3 for completeness.

3.2. ALMA CO Data

As introduced in Section 2.2, one spectral window of our ALMA observations was configured for observations of ^{12}CO ($1 - 0$) emission at 115 GHz. We utilize the ^{12}CO data to search for protostellar outflow signatures around the 5 ALMA detections which had no protostellar associations, as identified in Section 3.1. In summary, we find evidence for a protostellar outflow signature in only one of our imaged fields near source 5.

As shown in the left panel of Figure 2, source 5 shows red shifted and blue shifted CO emission perpendicular to the orientation of what appears to be a region of extended emission. The right panel of Figure 2 shows that both the red- and blue-shifted emission peaks are located about 3.5 km s^{-1} offset from the central source velocity, and additional emission extends at least another 7 km s^{-1} in the red-shifted emission, and up to 26 km s^{-1} in the blue-shifted material, suggesting the presence of outflowing gas.

Source 5 also contains two nearby protostellar sources found through the VISTA survey (Spezzi et al. 2015). The upper source, 054607.227-001134.91, is approximately $15''$ away from our detection, and is labeled as a Class II source (Spezzi et al. 2015), and was previously found by Flaherty & Muzerolle (2008) and Fang et al. (2009). The lower source, 054607.884-001156.83, is approximately $9''$ away from our detection, and is labeled as a potential Class III source (Spezzi et al. 2015).

Due to the absence of an associated infrared source at the location of source 5, this structure is likely a deeply embedded object, possibly a candidate first hydrostatic core. The first hydrostatic core stage is expected to have low-velocity molecular outflows at wide opening angles (Fujishiro et al. 2020), unlike the more collimated jets that accompany more mature protostellar sources. The velocity extent of the red-shifted material agrees well with the low-velocity ($1\text{-}10 \text{ km s}^{-1}$) molecular outflows

predicted from simulations (Machida et al. 2008), however, the velocity extent of the blue-shifted material is outside the expected range. Further observations are needed to confirm the precise evolutionary status of this source.

The lower nearby protostellar source in Figure 2, 054607.884-001156.83 (Spezzi et al. 2015), appears to lie along a region of extended emission, to the southeast of our ALMA detection. The extended emission features in our ALMA observations are very low-level, only reaching slightly above 1σ . Nonetheless these low-level features may be indicative of streamer-like objects spanning thousands of au, recently seen in other star forming systems (e.g., Pineda et al. 2020; Murillo et al. 2022; Pineda et al. 2023; Valdivia-Mena et al. 2023), or an envelope associated with filamentary structure (Tobin et al. 2010). Recent studies have also indicated that the presence of ring-like structures around protostellar sources could be caused by magnetic flux removal as dense cores collapse during early stages of star formation (Tokuda et al. 2023), which may also be morphologically consistent with our observations.

In order to verify that this emission is indeed real and potentially associated with a streamer, deeper kinematic measurements tracing the velocity structure are required. We do not pursue further analysis of this potential extended emission here.

3.3. Associations Summary

After consideration of the protostellar catalogs studied, with the addition of our ALMA observations in the CO, we classify sources 1, 4, 23, and 24 as likely being starless. The details of all of our associations are listed in Table 3.

As some analysis is dependent on accurate classification of the original NWT07 dense core population (see Section 4.3 for example), we perform the same check on that catalog for protostellar associations. We classify any protostellar object lying within $14''$ of the peak of the NWT07 core as associated, based on the beamsize of the SCUBA catalog. A total of 15 NWT07 SCUBA cores are re-classified as protostellar based on the catalogs studied, and will be used throughout the analysis when needed. In summary, we find that 58 fields are truly starless after verifying all ancillary data. This information is presented in Table 1, in the final column.

3.4. Candidate Starless Core Detections

Now we examine each of the four ALMA starless core detections in turn. Figure 3 shows source 1, the only candidate starless core detection that is centered on a SCUBA-based target. This detection lies in the central portion of the SCUBA dense core BN-546063-00935

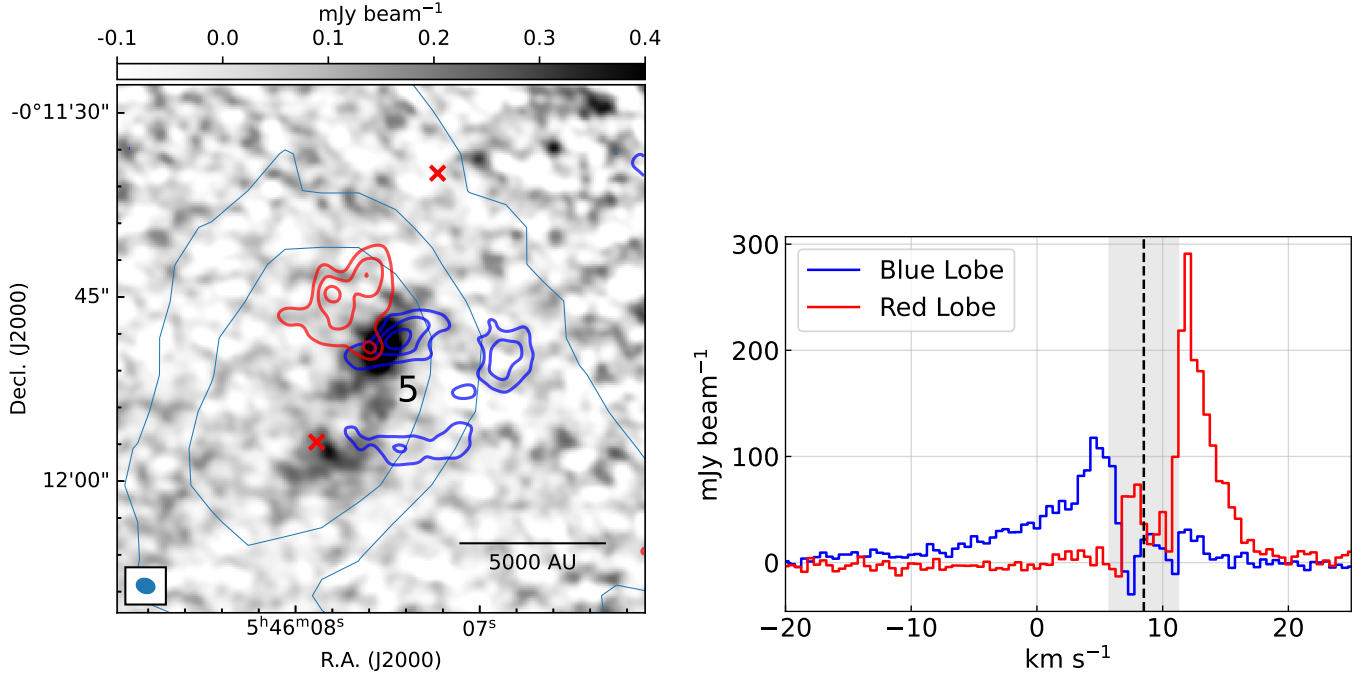


Figure 2. Left: Zoom-in of the upper region of ALMA field BN-546074-01342Mosaic with source 5 shown in the center (full mosaic shown in Figure 4). The grayscale ranges linearly from $-0.1 \text{ mJy beam}^{-1}$ to $0.4 \text{ mJy beam}^{-1}$, and the synthesized beam is given in the lower left corner within the frame. The light blue contours correspond to SCUBA2 $850 \mu\text{m}$ emission at the corresponding levels in mJy arcsec^{-2} : 0.15, 0.5, 1.0, 1.5, 3.0, 5.0. Protostellar sources in the field of view are plotted with red x markers. The blue and red contours represented velocity-shifted components of $^{12}\text{CO} (1-0)$, with integrated velocity ranges of -10 to 5.75 km s^{-1} and 11.25 to 16 km s^{-1} respectively. The aforementioned contours are shown at 3σ , 5σ , 7σ where the noise is $1\sigma \sim 0.150 \text{ Jy beam}^{-1} \text{ km s}^{-1}$. Right: Spatially-averaged spectrum within the 3σ contours of both red- and blue-shifted components as shown on the left. The grey shading indicates the velocity range excluded from the red and blue lobes, and the vertical black dashed line indicates the middle of this range. The lack of smaller-spacing data may be significantly filtering out emission within the velocity range indicated by the grey shaded region, near to the system velocity.

(NWT07) and has a detection significance of 8 times the local rms noise. The area surrounding the peak position of the detection is quite extended, and forms a larger area of diffuse emission. As highlighted in Section 3.1.2, our source 1 is associated with the ALMASOP core G205.46-14.56M3 (G205-M3). G205-M3 is the only core in the ALMASOP dataset that shows signatures of fragmenting substructure at a scale of 1000 au (Sahu et al. 2021). The emission is resolved into two noticeable substructures with diameters of 1755 au and 820 au, and are approximately separated by a distance of 1200 au (Sahu et al. 2021). Due to our lower sensitivity and resolution compared to Sahu et al. (2021), we are unable to resolve the two individual substructures within G205-M3. Nonetheless, Sahu et al. (2021) find that the enclosed masses, and their respective density profiles, are not consistent with a BE sphere-like model, and argue that this system likely represents an evolved starless state, just before the onset of star formation.

Figure 4 shows a newly detected starless core candidate, source 4, and all other protostellar cores which lie in the same mosaic. This source is one of the faintest sources detected in our sample, with a peak flux measurement of $0.45 \text{ mJy beam}^{-1}$, and has a detection significance of 7.4 times the local rms noise. This source is found to the south of multiple other protostellar sources in the SCUBA core BN-546074-01342, which have been positively identified as protostellar by Tobin et al. (2020) (see Table 3 for details).

It is striking that source 4 and the three previously identified protostellar sources appear regularly spaced along a line parallel to the elongation direction of the SCUBA emission, which is suggestive of formation via filament fragmentation (Pineda et al. 2023). This enhances the confidence of the source 4 detection despite its relatively low peak flux.

Figure 5 shows source 23 and 24, two additional newly detected fragments found within an area undergoing a

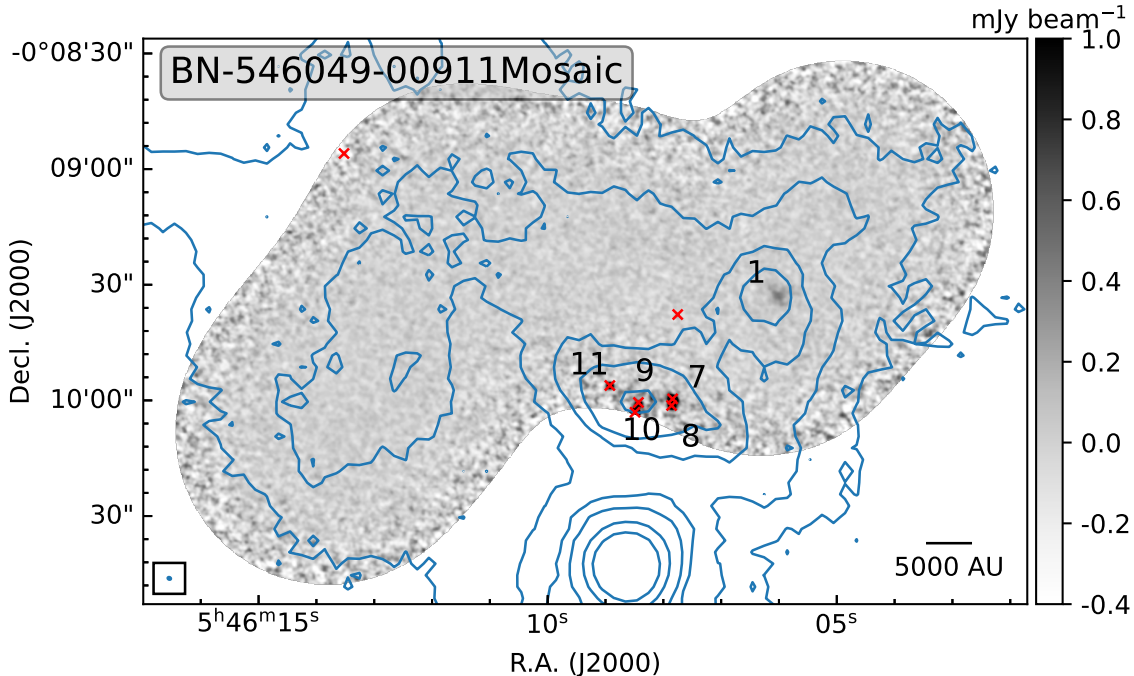


Figure 3. ALMA field BN-546049-00911Mosaic, with starless candidate source 1. The grayscale ranges linearly from $-0.5 \text{ mJy beam}^{-1}$ to $1.0 \text{ mJy beam}^{-1}$. The blue contours correspond to SCUBA2 $850 \mu\text{m}$ emission at the corresponding levels in mJy arcsec^{-2} : 0.15, 0.5, 1.0, 1.5, 3.0, 5.0. All detections are labeled in black with their respective index number. Protostellar sources in the field of view are also plotted with red markers (see Table 3 for details). The synthesized beam is plotted in the lower left corner within a frame, along with a scalebar, indicating a linear distance of 5000 au, at the assumed distance to Orion of 419 pc.

large amount of fragmentation. These detections are located quite offset from the center of the [NWT07](#) dense core BN-546450+00021. The larger area surrounding this dense core is home to a faint and complex emission structure, and more sensitive recent observations conducted by [Kirk et al. \(2016\)](#) indicate that there is a dense core associated with the positions of sources 23 and 24, with many individual fragmenting components¹. Note that the VANDAM protostellar survey (see Section 3.1.2) did cover the full region surrounding these detections with ALMA Band 7, but did not detect any emission for the locations associated with source 23 and 24. On the other hand, a recent 350GHz ACA Survey of 300 protostellar sources identified from the Herschel Orion Protostellar Survey was conducted by [Federman et al. \(2023\)](#). These observations trace the protostellar flux at the envelope scale ($\leq 8000 \text{ au}$), and find extended diffuse continuum detections at the locations of our source 23 and 24 ([Federman et al. 2023](#)). Thus, this region could very likely be at a moment in time where the transition

from the starless core stage into the protostellar stage is being directly observed and currently ongoing.

In summary, out of the 4 starless core candidates identified, only one is found to be directly associated with one of the starless cores in the [NWT07](#) sample. The other three all appear to be associated with fragmenting cores that already contain one of more protostellar sources.

4. DERIVED PROPERTIES

Table 4 lists the physical properties of each of the continuum sources, including the mass estimate, effective radius, and number density. The effective radius is computed from a geometric mean of the semi-major and semi-minor axes of the deconvolved size, and if the source is unresolved, the synthesized beam is used in place, and written as an upper limit.

4.1. Mass Estimates

We estimate the mass of each continuum source using the standard equation:

$$M = 100 \frac{d^2 S_\nu}{B_\nu(T_D) \kappa_\nu}, \quad (1)$$

¹ See Appendix A regarding the differences between the SCUBA and SCUBA-2 core catalogs for Orion B North.

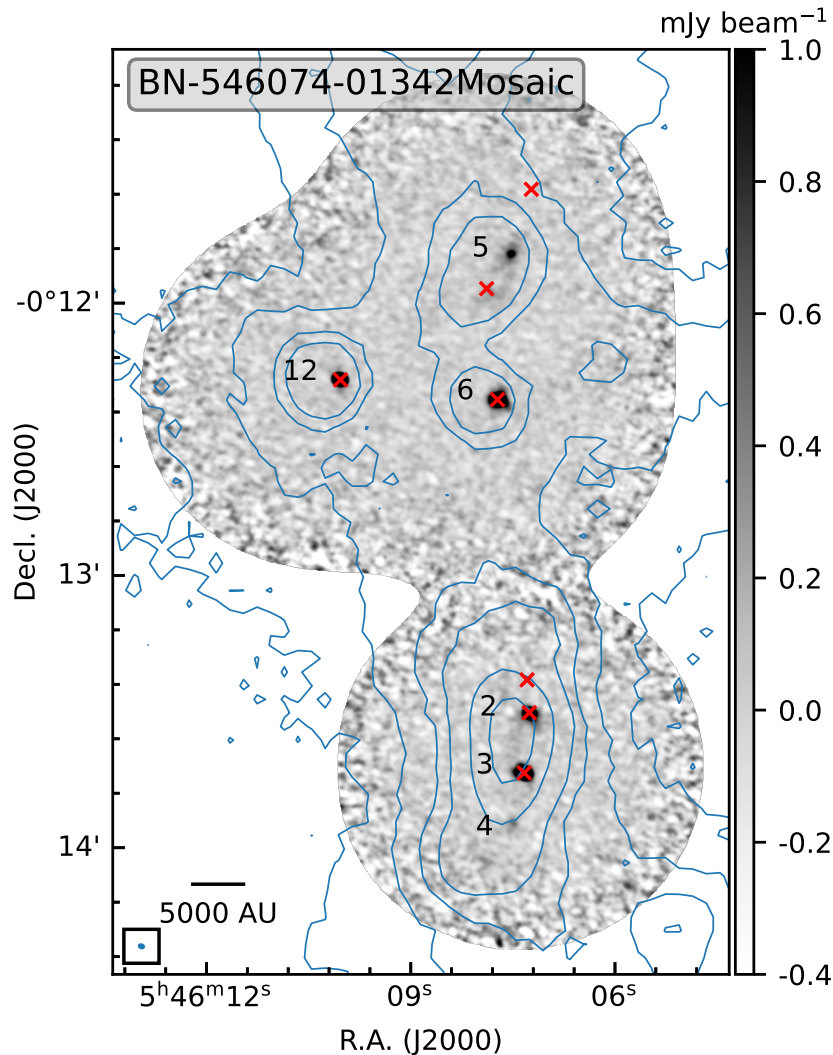


Figure 4. ALMA field BN-546074-01342Mosaic, with starless candidate source 4. See Figure 3 for plotting conventions.

where d is the distance, S_ν is the integrated flux at frequency ν , B_ν is the Planck function at the dust temperature of T_D , and the factor of 100 represents the gas-to-dust ratio. We adopt a slightly updated value of distance, $d = 419$ pc, consistent with newer estimates from Zucker et al. (2019), along with a core temperature of $T = 10$ K.

We use commonly adopted calculations of opacities, Ossenkopf & Henning (1994), specifically the OH5 model corresponding to thin ice mantles after 10^5 years of coagulation at a gas density of 10^6 cm^{-3} . Extending the model to an effective frequency of 106 GHz yields our choice in opacity of $\kappa_\nu = 0.23$ cm^2 g^{-1} . As mentioned in Dunham et al. (2016), specific choices in opacity typically have uncertainties of factors 2–4 (see also Shirley et al. 2005, 2011) along with additional uncertainties in the power-law index due to dependence on grain size

(Ricci et al. 2010a,b; Tobin et al. 2013; Schnee et al. 2014; Testi et al. 2014). Since the mass is inversely proportional to κ , reducing κ to half the value we presently adopt (as is used in Motte et al. 1998) would increase masses by a factor of two.

We calculate the mean density of each source as

$$n = \frac{3}{4\pi\mu m_{\text{H}}} \frac{M}{R_{\text{eff}}^3}, \quad (2)$$

where $\mu = 2.80$ is the mean molecular weight per hydrogen molecule (Kauffmann et al. 2008) and m_{H} is the mass of a hydrogen atom. Both the computed mass and number density estimates are given in Table 4. The uncertainties are dominated by systematic effects (such as temperature, distance, dust opacity, etc.), rather than the statistical uncertainties associated with the Gaussian fits performed to characterize the size of the sources.

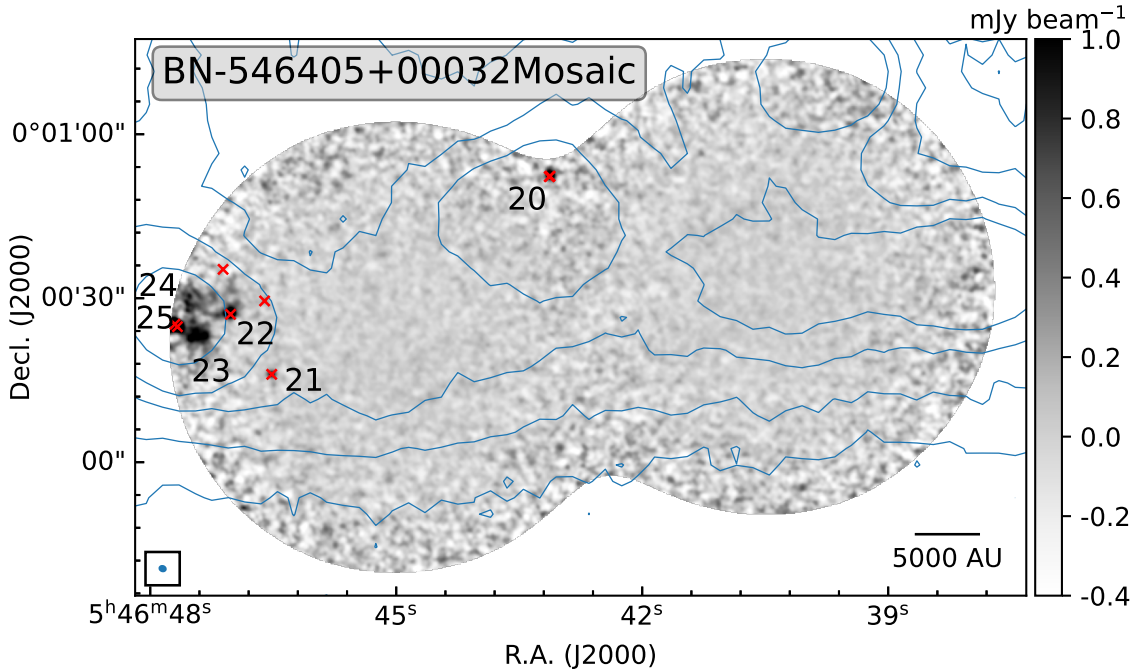


Figure 5. ALMA field BN-546405+00032Mosaic, with starless candidates sources 23 and 24. See Figure 3 for plotting conventions.

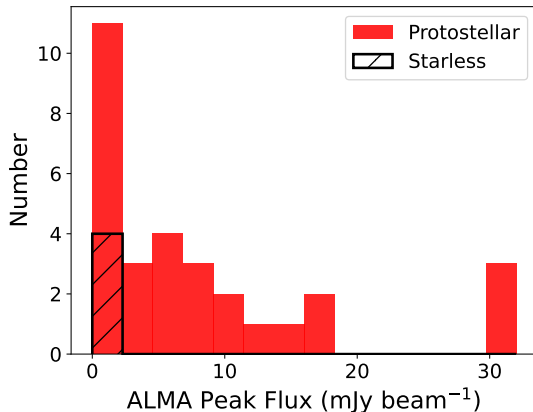


Figure 6. Distribution of ALMA detection peak fluxes. Detections with a peak flux greater than 30 mJy beam^{-1} are plotted in the final bin shown. We show both the protostellar ALMA detections in red (30 sources total), along with the candidate starless core detections in black (4 sources total).

4.2. ALMA Peak Flux

Figure 6 shows the distribution of peak fluxes for both the protostellar and starless population of our ALMA detections. It is expected that the later stages of prestellar core evolution passes relatively quickly (Jessop & Ward-Thompson 2000; Girichidis et al. 2014; Zamora-Avilés & Vázquez-Semadeni 2014), in which the stage at which the prestellar core is detectable. Compared to the development of a protostellar core, a starless core

typically has a lower central density, and as a result, we should expect to see our prestellar cores have a low peak flux compared to the protostellar cores in our sample. All of our starless core detections notably lie in the lowest peak flux bin, suggesting that our observations agree with the overall picture of starless core evolution.

4.3. SCUBA Core Concentration

We measure the central concentration of dense cores from the NWT07 catalog, with the following definition:

$$C = 1 - \frac{1.13B^2F_{\text{tot}}}{\pi R^2F_{\text{pk}}}, \quad (3)$$

where B is the beamsize, F_{tot} is the integrated flux, R is the effective radius, and F_{pk} is the peak flux (Johnstone et al. 2000).

The importance of self-gravity alongside the internal pressures of dense core structure, set the possible collapse of these structures into the smaller scales, usually associated with protostars. Bonnor-Ebert spheres (BE Spheres) are a spherical, isothermal model for self-gravitating pressure-confined objects (Ebert 1955; Bonnor 1956), and this simple model predicts a range of values in terms of central concentrations. It is expected that dense cores become more centrally concentrated as they evolve in time, with uniform spheres having a central concentration value of 0.33 while the central concentration value of 0.72 is the maximum allowed for a stable BE sphere (Johnstone et al. 2000). Any cores above such

Table 4. Physical Properties of Detections

Src ^a	Mass	R_{eff}	Number Density		
#	(M_{\odot})	(au)	(cm ⁻³)		
(1)	(2)	(3)	(4)	(5)	(6)
1	0.64	...	1010	...	1.9e+07
2	1.69	...	170	...	1.1e+10
3	5.10	...	130	...	7.2e+10
4	0.19	...	410	...	8.3e+07
5	0.72	...	620	...	9.1e+07
6	3.00	...	220	...	8.7e+09
7	1.05	...	110	...	2.1e+10
8	0.48	...	150	...	4.6e+09
9	0.76	...	680	...	7.4e+07
10	1.04	<	290	>	1.2e+09
11	0.32	...	90	...	1.3e+10
12	5.57	...	50	...	1.3e+12
13	1.55	...	120	...	2.4e+10
14	0.07	<	290	>	8.8e+07
15	10.18	...	110	...	2.6e+11
16	0.25	...	130	...	3.4e+09
17	0.07	<	290	>	8.0e+07
18	2.42	...	350	...	1.8e+09
19	3.46	...	200	...	1.2e+10
20	0.33	...	170	...	2.1e+09
21	0.14	<	290	>	1.7e+08
22	0.49	...	250	...	9.7e+08
23	1.72	...	960	...	5.9e+07
24	1.07	...	840	...	5.5e+07
25	1.00	...	170	...	6.3e+09
26	0.35	...	310	...	3.5e+08
27	0.59	...	140	...	6.3e+09
28	1.29	...	450	...	4.3e+08
29	0.96	...	180	...	4.8e+09
30	2.25	...	170	...	1.4e+10
31	0.37	...	170	...	2.1e+09
32	7.06	...	440	...	2.5e+09
33	0.99	...	150	...	8.1e+09
34	1.42	...	140	...	1.6e+10

^aRunning Index Number, the same as Table 2.

NOTE—(3) and (5) show limit indicators for unresolved sources. For these sources, the synthesized beam has been used in-place for the size; the effective radius should be taken as an upper limit, while the number density should be taken as a lower limit.

a value do not have equilibrium solutions, and therefore must undergo gravitational collapse. Dense cores that are high in central concentration are usually found to be protostellar in nature (e.g., [Johnstone et al. 2000](#); [Kirk et al. 2006](#); [Jørgensen et al. 2008](#)).

Figure 7 shows the distribution of central concentration for all [NWT07](#) cores in Orion B North. There are six starless dense cores that have concentrations lower than 0.33, the minimum value allowed for a uniform

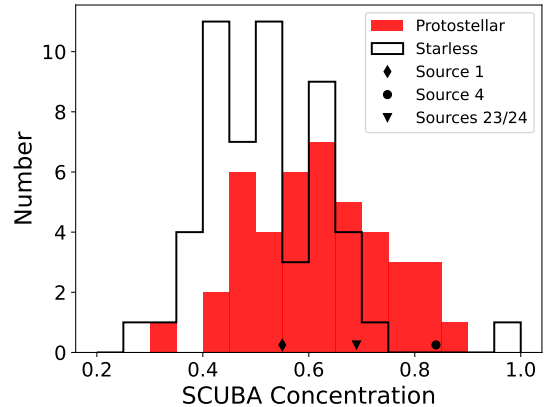


Figure 7. Distribution of core concentrations for dense cores in the Orion B North star forming region, computed from the re-classified [NWT07](#) catalog (see Section 3.3 for details). See Figure 6 for plotting conventions. Markers indicate the concentrations of the parents core of the associated labeled candidate starless core(s). We have excluded all values below a concentration of 0.2 (see Section 4.3 for discussion regarding this choice).

sphere. The [NWT07](#) catalog for the Orion B North area, has a reported 1σ rms of 16 mJy beam^{-1} , and the analysis uses a detection threshold of $> 5\sigma$ relative to the local background for a robust source classification. Due to the lack of precision published in the values for the peak flux and the integrated flux ([NWT07](#)), for values of emission near the lowest reported limit of 0.1 Jy beam^{-1} , there exists a large amount of uncertainty. Since the central concentration uses both the measure of peak flux, as well as the total integrated flux, for the faintest cores, associated errors and uncertainties would propagate much more significantly. In this case, some reported values are found below the allowed minimum value of 0.33.² The surprisingly high concentration value of 0.955 associated with a starless core (the most elongated core reported in the [NWT07](#) sample) similarly appears to be influenced by the same reasons as above. In all cases, the associated SCUBA-2 dense cores do have concentrations above the minimum 0.33 ([Kirk et al. 2016](#)) (see Appendix A for discussion).

Our starless core candidates lie in SCUBA dense cores with concentration values of 0.55 (source 1), 0.84 (source 4), and 0.69 (sources 23 and 24). While there is a range of concentrations for both the starless and pro-

² Additionally, for cores in close proximity to other cores in the catalog, [NWT07](#) necessarily reduced the elliptical aperture size used to perform the 2D fit, to a level below the usually chosen 3σ contour. This choice partitions the extended emission between the cores, and could also contribute to the overall uncertainty in the measurements reported.

tostellar population of cores, as seen in Figure 7, more starless cores are found at lower concentrations, as expected for starless core populations in which they are more likely found in areas of extended emission still undergoing mass accretion and gravitational collapse. We find that our starless core detections are either within the typical range for protostellar dense cores, or on the higher side for starless dense cores.

In the analysis of the Ophiuchus molecular cloud, Jørgensen et al. (2008) found four starless cores with a high degree of central concentration, contrary to the previous study in the Perseus molecular cloud, where no starless cores were found to have a central concentration higher than 0.6 (Jørgensen et al. 2007). Kirk et al. (2017a) subsequently found no ALMA detections for SCUBA starless cores in Ophiuchus with concentrations below 0.6, but did detect all starless cores with higher concentrations than 0.6. Further evolved starless cores are expected to have a higher degree of central concentration as they collapse towards a protostellar state. All of our starless cores detections exhibit a high degree of central concentration, reinforcing this picture.

5. SUBSTRUCTURE AND FRAGMENTATION IN STARLESS CORES

5.1. Numerical Simulations and Synthetic Observations

Turbulent simulations predict that fragmentation within dense cores begins during the starless core phase (Offner et al. 2012). Interferometers like ALMA are uniquely suited to detecting these small and faint density peaks within starless cores, while simultaneously filtering out larger-scale emission structures. In this section, we perform the same approach as Dunham et al. (2016) and Kirk et al. (2017a), and compute the number of starless core detections predicted by the turbulent fragmentation model for our observed Orion B North core sample.

We use magneto-hydrodynamic simulations of isolated, collapsing starless cores, with an initial core mass of $0.4M_{\odot}$, using the ORION Adaptive Mesh Refinement (AMR) code base (Li et al. 2021), to generate self-consistent, time-dependent physical conditions. The simulation starts with a uniform density spherical core of gas, at a temperature of 10 K, with an initial number density of $1.6 \times 10^5 \text{ cm}^{-3}$ and uniform magnetic field in the z direction (e.g., similar to Offner & Chaban 2017). The core is surrounded by a warm, low density medium, with a temperature of 1000 K, and a density 100 times lower than the initial core density. At the starting time step in the simulation, the gas velocities in the core are perturbed with a turbulent random field, and once set in

motion, are allowed to decay with no additional energy injection. ORION evolves the calculations until shortly after the formation of a first hydrostatic core, which is represented by a sink particle. For more in-depth details on the descriptions of the simulations, we refer to the reader to Section 5.1.1 in Dunham et al. (2016).

To generate synthetic ALMA observations, we use the same turbulent simulation snapshots as in Dunham et al. (2016) and Kirk et al. (2017a). We take the total gas column density snapshots and convert them to total gas surface density, using the same mean molecular weight per free particle as in Equation 2. We then derive the mass in each pixel, and compute the flux map using Equation 1.

Finally, we create the synthetic observations using the appropriate antenna configurations, on-source time, and distance to Orion B North to match our current ALMA observations. The synthetic observations were generated using CASA’s `simalma` task, and re-imaged with CASA’s `tclean` task to mimic all imaging parameters used in the physical observations (see Section 2.2 for details). We choose the position of R.A. = 05:47:00 and Decl. = +00:05:00 for our simulated observations, which equates roughly to the center of our observational area in Orion B North. We use a total on source time of 270 s, with 190 s at the more compact configuration, and 80 s at the more extended configuration, to match our real observations. We use integration times of 2 s at an effective mean frequency of 106 GHz with a bandwidth of 6 GHz, include the default atmospheric noise model, and the same imaging cell size of $0.17''$ used to image the real observations.

Figure 8 shows six time steps (from 0.129 Myr to 0.171 Myr) of the synthetic ALMA observations of the $0.4M_{\odot}$ core simulation.

5.2. Detecting Starless Cores

With the assumption of a continuous rate of star formation over the timescale at least as long as the core lifetimes, then similar to Dunham et al. (2016) and Kirk et al. (2017a), we can compute the expected number of detections as the following:

$$\text{Detections} > \frac{2}{3} \times N_{\text{total}} \times \left(\frac{n_{\text{Detectable}}}{n_{\text{Limit}}} \right)^{-0.5}, \quad (4)$$

where N_{total} is the number of starless cores observed, $n_{\text{Detectable}}$ is the core density at which our ALMA observations can detect the core, and n_{Limit} is the observed lower limit of the mean core densities as observed at single-dish resolution (in this case, the NWT07 data).

Figure 9 shows the distribution of core number densities for all cores in the Orion B North star forming re-

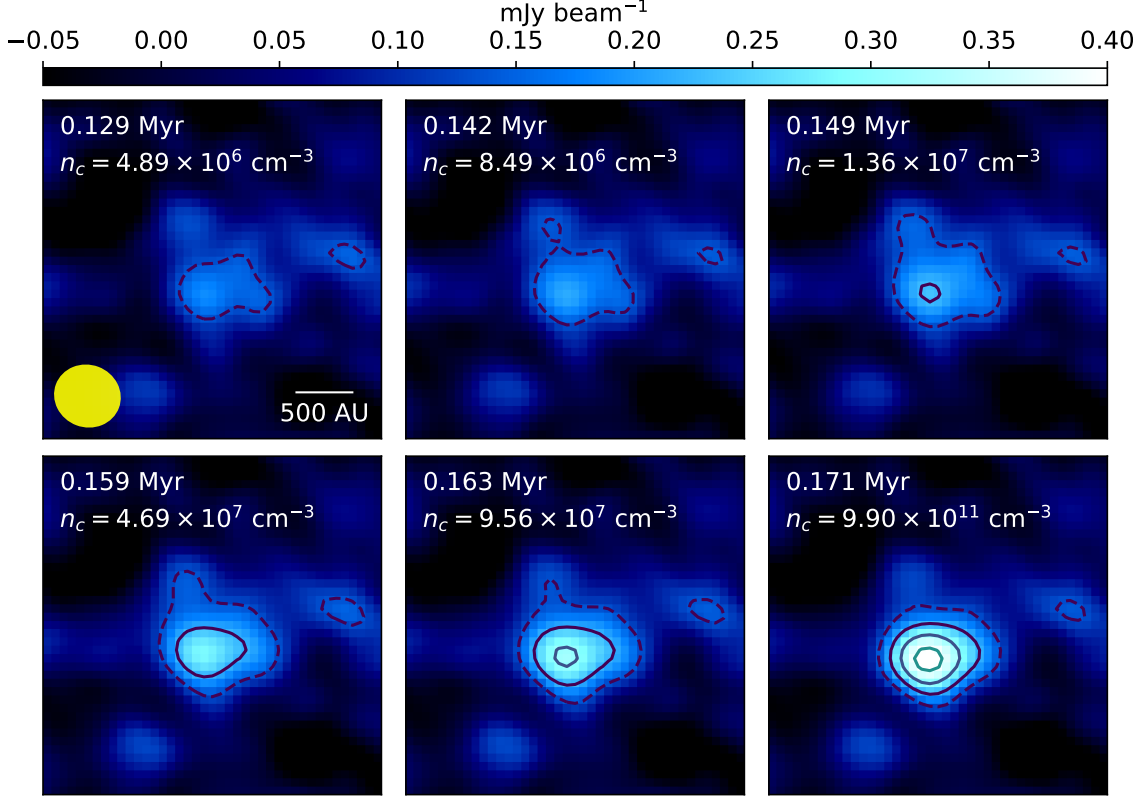


Figure 8. Synthetic ALMA 106 GHz observations of the $0.4M_{\odot}$ simulation, at six given timesteps, indicated in each panel along side the central density of the core. The synthesized beam is given in the first panel as a yellow ellipse in the bottom left corner. The dashed contour represents the 3σ level. The solid contours start at a level of 5σ and increase by 2σ , where $1\sigma \sim 0.045 \text{ mJy beam}^{-1}$. We consider a robust detection to be a minimum of 5σ .

gion as presented in [NWT07](#). The lowest density cores found in our population, near the left tail of the distribution (along with the one significant outlier) correspond to cores with atypical properties (highly elongated and very large cores), so we briefly explain our choice for the observed lower limit chosen for our calculations³. We compute the number density of a dense core whose size is equal to the beamsize ($14''$) and which lies at the sensitivity limit of the [NWT07](#) dataset, to represent an object at the minimum detectable density. [NWT07](#) classifies any object at 5σ above the local noise level as a positive detection, and for the Orion B North area, the 1σ rms noise is given as 16 mJy beam^{-1} . This corresponds to a minimum detectable density of $2.11 \times 10^4 \text{ cm}^{-3}$. For comparison, our lowest density starless core observed has an estimated density of $5.68 \times 10^3 \text{ cm}^{-3}$, although as can be seen in [Figure 9](#), only a small number of the starless cores have estimated densities below $2.11 \times 10^4 \text{ cm}^{-3}$. Our derived value of $2.11 \times 10^4 \text{ cm}^{-3}$

³ The most atypical core, BN-547034+1950, is the same extremely high concentration core as detailed in [Section 4.3](#).

agrees well with the lower tail of the distribution as shown in [Figure 9](#), and is representative of a typical core seen in our observations.

The central core peak in the simulations is only detected at a 5σ level after 0.149 Myr, when the central core density reaches $1.36 \times 10^7 \text{ cm}^{-3}$. We use this as the criteria for a robust detection, and we set the detectability limit as such.

In total, for the Orion B North region studied, we have $N_{\text{total}} = 58$ starless cores (as re-classified in [Section 3.3](#)), with a minimum density of $n_{\text{Limit}} = 2.11 \times 10^4 \text{ cm}^{-3}$, along with the detectability limit of our ALMA configuration $n_{\text{Detectable}} = 1.36 \times 10^7 \text{ cm}^{-3}$. Using [Equation 4](#), along with Poisson statistics, we predict a minimum of $2 (1.52) \pm 1$ starless cores that have enough substructure for a positive detection in our observations.

As shown in [Figure 9](#), there exists a small number of starless cores that have estimated densities lower than our chosen density limit. For example, our lowest estimated density core with a density of $5.68 \times 10^3 \text{ cm}^{-3}$ belongs to the same highly elongated core as mentioned earlier in this section. If we instead utilize this density in place of our chosen density limit, we would lower our

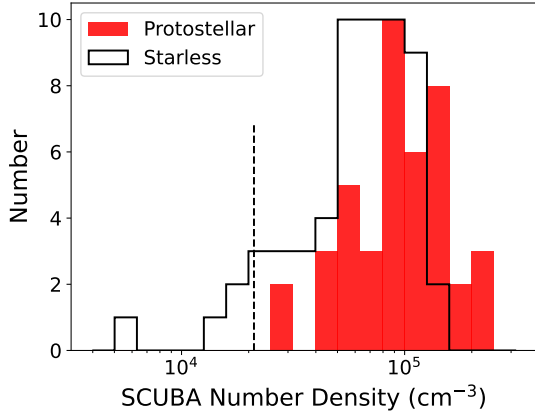


Figure 9. Distribution of NWT07 core number densities. The black histogram indicates cores classified as starless, while the red filled histogram indicates cores classified as protostellar in nature. The vertical black dashed line indicates the minimum detectable density, as computed in Section 5.2.

expected number of starless core detections to 0.79. The results would remain unaffected with either difference in chosen detectability limit.

For completeness, we also consider the potential uncertainty in the total number of cores observed, for example, if the NWT07 catalogue over-segmented cores lying within filamentary structure. As described in Appendix A, we perform a careful visual comparison between the NWT07 core catalog with the core catalog of Kirk et al. (2016) of the same region using newer SCUBA-2 data and an independent core-identification technique. While the vast majority of the cores identified agree well, we note several instances where the two catalogs differ. Conservatively, we estimate that the true number of starless cores observed from the NWT07 catalog lies between 47 and 61. This range places the number of predicted detections between 1.23 and 1.60.

In addition, we note that various dust and gas tracers used for core identification can lead to differences in the boundaries of identified cores (e.g., Ikeda et al. 2009), leading to further uncertainties in the total number of cores observed, which could increase the range in true core numbers reported above.

Due to the re-classification of the original NWT07 SCUBA core catalog, only one of our total four starless core candidates lie in a truly starless dense core (see Section 3.3). Thus, we show that this one starless core detection is consistent with the model predictions. Additionally, we also run the same synthetic observations on the simulation of a $4M_{\odot}$ starless core and find less than a factor of two difference in the detectability threshold despite the change in initial mass of an order

of magnitude, suggesting a similar number of detections (1.23) (see Appendix B for details).

As introduced in Section 1, a BE sphere-like model has a smooth and broad density profile, as driven by completely thermal evolution processes. Observations taken with an interferometer leads to filtering effects, which depending on the scale of emission, can impact the detectability of such objects. Dunham et al. (2016) demonstrated that structures generated from the collapse of turbulent cores should be detectable at a rate approximately 100 times higher than the BE sphere-like model for their ALMA observational setup of Chamaeleon I. Since our ALMA observations are very similar to those taken in both the Chamaeleon I ALMA study (Dunham et al. 2016) and the Ophiuchus ALMA study (Kirk et al. 2017a), we should also expect to see a lack of detections if the evolution and resulting density structure is similar to that of a BE sphere-like model.

A single detection under the turbulent fragmentation model is not a large number for model testing, however, we note that under the BE sphere-like model, it would be very unlikely to get a single detection. With the combination of Orion B North and Ophiuchus (Kirk et al. 2017a), we now have two studies which show that the fragmentation model serves to represent a clearer picture of the on-going evolution of starless core evolution.

5.3. Evolutionary Lifetime Estimate

Relative source counts are a popular way to estimate the lifetime of the earlier phases of star formation (e.g., Beichman et al. 1986; Jessop & Ward-Thompson 2000; Kirk et al. 2005). Assuming a continuous star formation rate, the ratio of lifetimes of earlier and later phase objects is directly reflected in the relative number counts. Many measures for nearby star forming regions currently exist with central densities between $\sim 10^3$ and $\sim 10^5$ (see review by Ward-Thompson et al. 2007). We can apply a similar procedure for our single ALMA detected starless core to obtain a crude estimate at slightly higher central densities, noting the inherently large uncertainty with only one starless core detected in our sample.

We adopt a reference Class I protostellar lifetime of 0.74 Myr from Könyves et al. (2015) derived from relative protostellar counts of Spitzer data of Orion B (Megeath et al. 2012). By comparing the 37 Class I cores found within the NWT07 survey footprint from the SESNA catalog (R. Gutermuth et al. 2024, in preparation) to our one ALMA starless core detection, we estimate the lifetime for ALMA detectability to be 2.0×10^4 yr.

Our starless core has an estimated central density of 1.86×10^7 cm⁻³, implying a free-fall timescale of

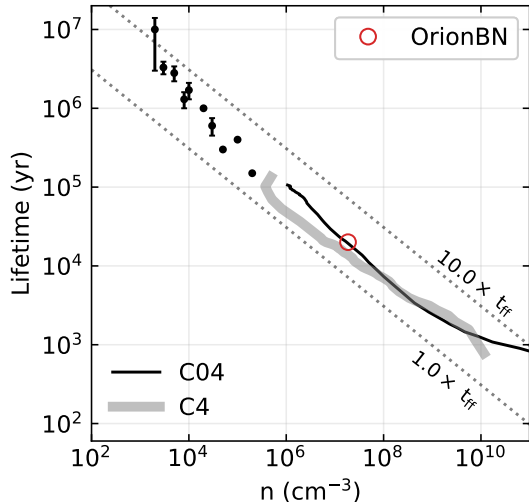


Figure 10. Lifetimes vs. central number densities for the $0.4M_{\odot}$ simulation (C04) and the $4.0M_{\odot}$ simulation (C4), as reproduced from Figure 10 in Dunham et al. (2016). The lifetime at each given density is the amount of time it takes the simulation to evolve from that given timestep to the onset of the first hydrostatic core phase. The dashed lines indicate the free-fall lifetime ($t_{ff} = \sqrt{3\pi}/(32G\rho)$) and $10t_{ff}$. The data points show early sub-mm observations at smaller densities (see Jessop & Ward-Thompson 2000; Kirk et al. 2005). The red circular marker shows the statistical lifetime derived with the Orion BN ALMA observations.

7.12×10^3 yr. As shown in Figure 10, our estimated ALMA-detected starless core lifetime is larger than this free-fall timescale by a factor of 2.80, however, we emphasize the large uncertainties associated with our estimate given that we only have one detection. We interpret our result as implying the core lifetime at a density of approximately 10^7 cm^{-3} is more consistent with a shorter timescale (i.e., closer to the free-fall time) rather than a longer timescale (i.e., closer to 10 times the free-fall time), and note that a larger sample size is necessary to get a firmer lifetime estimate. The shorter lifetime for our ALMA detection is consistent with the numerical simulations, that we analyze, where the lifetimes tend to lie closer to t_{ff} than $10 \times t_{ff}$.

6. COMPARISON TO CHAMAELEON I AND OPHIUCHUS

Through the analysis of the Chamaeleon I star forming region, Dunham et al. (2016) expected two starless core detections under the turbulent fragmentation model, but found no such detections in their observations. Dunham et al. (2016) proposed three arguments as to why no starless core detections were found in the Chamaeleon I cloud: the lack of continuous star formation in the cloud, that the assumption of the core

lifetime proportionality to the free-fall time is not correct, or that the numerical simulations are not applicable. This is in direct contrast to the study performed by Kirk et al. (2017a), where the dense core population of the Ophiuchus star forming region was analyzed, and found to agree with those same fragmentation models with two tentative detections compared with two predicted.

With the addition of the Orion B North observations, we are now in a position to search for differences in the core populations per cloud, as a possible explanation for the lack of detections in Chamaeleon I. A basic virial analysis was performed by Tsitali et al. (2015) in which the core’s self-gravity contribution is compared with the thermal and non-thermal pressure support within the core. From this analysis, Tsitali et al. (2015) showed that the population of dense cores in the Chamaeleon I cloud are gravitationally unbound, suggesting that star formation may not continue.

A full virial analysis allows for more information regarding specific physical processes that may be guiding differences in star forming regions. Some additional virial terms are pressure support from cloud-wide turbulence, pressure support from the molecular cloud weight, and contributions from magnetic fields (e.g., Pattle et al. 2015; Kirk et al. 2017b; Kerr et al. 2019).

We carry out both the simple Jeans analysis and a fuller virial analysis including the larger-scale external pressure binding terms, to investigate the difference in the predicted number of detections between the star-forming clouds studied. Since our goal is to compare the core populations between clouds, we adopt comparable datasets for all three clouds; unfortunately no such uniform data was available for the magnetic field strength, so we exclude this term. We follow with descriptions of the adopted comparable datasets as they pertain to both the Jeans analysis and the fuller virial analysis.

6.1. Datasets Used

6.1.1. Dust Continuum-based Properties - Mass and Size

We adopt the dataset from Belloche et al. (2011) for the Chamaeleon I cloud, Jørgensen et al. (2008) for Ophiuchus, and NWT07 for Orion B North, which are sub-millimetre dust continuum observations from single dish telescopes deriving the mass and size of the dense core population.

Chamaeleon I observations were conducted with the LABOCA bolometer array on the APEX telescope, measuring the dust continuum at $870 \mu\text{m}$ (Belloche et al. 2011). Cores were identified using Gaussclumps (Stutzki & Guesten 1990; Kramer et al. 1998), on the

continuum maps of Chamaeleon I produced by [Motte et al. \(1998, 2007\)](#).

Both the Ophiuchus and Orion B North datasets were observed with the SCUBA instrument on the JCMT at a wavelength of $850 \mu\text{m}$ ([Nutter & Ward-Thompson 2007](#); [Jørgensen et al. 2008](#)). In the case of Ophiuchus, the core finding algorithm `clumpfind` was utilized ([Williams et al. 1994](#)) and the core sizes were estimated based on the number of pixels contained within the `clumpfind` core boundary. For Orion B North, [NWT07](#) estimated the core sizes, in most cases, by placing an elliptical aperture on each source and approximately matched to the position of the 3σ contour. We directly adopt the masses and sizes as reported in these aforementioned papers for our analysis.

6.1.2. Dense Gas Kinematics

NH_3 and similar other N-bearing species are often found to be a good tracer of dense core material and can usually probe deeper layers than similar measurements conducted with C-bearing species (e.g., [Jijina et al. 1999](#); [di Francesco et al. 2007](#)). These measurements provide similar measures of kinematic core properties across different star forming environments ([Johnstone et al. 2010](#)). The Green Bank Ammonia Survey (GAS, [Friesen et al. 2017](#)) mapped $\text{NH}_3(1,1)$ and $\text{NH}_3(2,2)$ in the Orion B North and Ophiuchus clouds, providing measurements of the dense gas excitation temperature and thermal and non-thermal components of the line width.

[Tsitali et al. \(2015\)](#) observed many different spectral lines in the Chamaeleon I cores; we adopt the $\text{N}_2\text{H}^+(1-0)$ data as being the most comparable to the NH_3 data available for the other two clouds. In the study of dense gas tracers in Perseus, [Johnstone et al. \(2010\)](#) show that the kinematic properties of $\text{NH}_3(1,1)$ and $\text{N}_2\text{H}^+(1,0)$ are extremely similar, showing that these species are well coupled, regardless of the physical conditions in the dense core gas. This reinforces our choice to only use the $\text{N}_2\text{H}^+(1-0)$ for the Chamaeleon I region. We assume a dense core gas temperature of $T = 10 \text{ K}$ for the Chamaeleon I cores, the same as [Tsitali et al. \(2015\)](#).

6.1.3. Larger Scale Turbulent Material

The turbulent motions present in the lower density material surrounding the dense cores is often traced by various CO isotopologues. The all-sky CO surveys⁴ using the CfA and Cerro Tololo telescopes provides the

best source of comparable CO data across all three regions studied ([Dame et al. 2001](#); [Dame & Thaddeus 2022](#)). We choose to utilize the newer Northern Sky Survey of [Dame & Thaddeus \(2022\)](#), which is a large extension of the Galactic plane CO survey of [Dame et al. \(2001\)](#) to the entire northern sky ($\delta > -17^\circ$). This survey uniformly samples the high-latitude sky with a resolution of 0.25 degrees, along with spectra with uniform sensitivity of 0.18 K in 0.65 km s^{-1} channels across a velocity range of $\pm 47.1 \text{ km s}^{-1}$. We expect these contributions to lead to an overestimate of the associated linewidth due to the coarse spectral resolution; we discuss these implications in Section 6.4.

6.1.4. Cloud Weight

Finally, we utilize the all-sky dust extinction maps of [Rowles & Froebrich \(2009\)](#) to estimate the compression on the dense cores due to the weight of their surrounding molecular cloud. We use the $N = 25$ star maps to maximize the angular resolution available (see Section 2.1 in [Rowles & Froebrich 2009](#)).

6.2. Data Coverage

The chosen extinction and ^{12}CO maps are all-sky, therefore have uniform coverage over all three clouds studied. The dense gas tracers, NH_3 and N_2H^+ , are more limited in terms of area mapped and area detected. We briefly explain the kinematic dataset coverage with respect to each dense core population studied.

6.2.1. Ophiuchus

GAS provides measurements of the dense gas line width and temperature, however, the latter quantity covers a smaller area as the fainter $\text{NH}_3(2,2)$ line needs to be detected in addition to the $\text{NH}_3(1,1)$ transition. In order to maximize the kinematic data available, we assume a temperature of $T = 13 \text{ K}$ for all cores that have only line width information available (taken as the mean temperature for all dense cores covered by GAS, in Ophiuchus). In Ophiuchus, 55 of the 66 dense cores, or 83% have GAS line width measurements, with a subset of 29 cores containing kinetic temperature measurements. This dataset represents the largest overlap with the GAS kinematic data in our three cloud comparison.

Virial analyses of Ophiuchus based on SCUBA-2 data, have recently been published ([Pattle et al. 2015](#); [Kerr et al. 2019](#)), however, for consistency with the SCUBA-based core catalogue used for the ALMA survey, we run our own independent analysis.

6.2.2. Orion B North

In Orion B North, only 18 of the 58 dense cores, or 31% have GAS line width measurements, with a sub-

⁴ The CO Survey Archive is found at the following: <https://lweb.cfa.harvard.edu/rtdc/CO/>

set of 16 cores containing kinetic temperature measurements. The GAS mapping of Orion B North appears incomplete, resulting in a low amount of coverage in comparison to Ophiuchus. We note that the 16 cores with kinematic information available for this analysis are representative of the overall dense core population in Orion B North. We assume a temperature of $T = 15$ K for all cores which only have line width measurements (again taken as the mean temperature for all dense cores covered by GAS, in Orion B North).

6.2.3. *Chamaeleon I*

In Chamaeleon I, 19 of the 60 dense cores, or 33%, are detected in the $\text{N}_2\text{H}^+(1-0)$ line (Tsitali et al. 2015). Tsitali et al. (2015) do detect many more of the cores in lower density gas tracers, however, as noted in Section 6.1.2, we adopt only the $\text{N}_2\text{H}^+(1-0)$ data, as being the most comparable to the data available in the other two regions.

In total, we present the 19 dense cores in Chamaeleon I, 55 dense cores in Ophiuchus, and 18 dense cores in Orion B North, for a total of 92 dense cores in our virial analysis. We utilize the protostellar re-classification conducted by Dunham et al. (2016) for Chamaeleon I, Kirk et al. (2017a) for Ophiuchus, and this work for Orion B North (see Table 1 and Section 3.3) to separate the dense core population into starless cores and protostellar cores as needed for the analysis.

6.3. *Jeans Analysis*

We first compute the virial parameter, α , which indicates the relative contribution of self-gravity versus that of thermal and non-thermal support. It is computed for a uniform, ellipsoid source, following the standard method outlined in Bertoldi & McKee (1992):

$$\alpha = \frac{5\sigma_{\text{tot}}^2 R}{GM}, \quad (5)$$

where R is the core radius, G is the gravitational constant, and M is the core mass. The total velocity dispersion, σ_{tot} , is given by the following:

$$\sigma_{\text{tot}} = \sqrt{(\sigma_{\text{obs}}^2 - \sigma_{\text{th,mol}}^2 + \sigma_{\text{th,mean}}^2)}, \quad (6)$$

with σ_{obs} representing the observed dense gas line width. The mean and molecular velocity dispersions are calculated as follows:

$$\sigma_{\text{th,mean}} = \sqrt{\frac{k_B T}{\mu m_H}}, \quad (7)$$

$$\sigma_{\text{th,mol}} = \sqrt{\frac{k_B T}{m_{\text{mol}}}}, \quad (8)$$

where the molecular weight of the mean particle is μm_H ($\mu = 2.37$), and $m_{\text{mol}} = \mu_{\text{mol}} m_H$ is the molecular mass of the tracer, in this case NH_3 . As highlighted in Section 6.1.2, we compute these values for the Orion B North and Ophiuchus regions from the GAS data. We use the fitted line width and temperature values for the pixel that the core's peak lies within, where available. We utilize the published values by Tsitali et al. (2015) for their pointed observations of the Chamaeleon I cores from Belloche et al. (2011) and assume the same temperature of $T = 10$ K, as outlined in Section 6.1.2.

Figure 11 plots the virial parameter against the core mass for all three core populations. None of the Chamaeleon I dense cores fall below the dashed line, indicating that all cores are gravitationally unbounded under this simple virial analysis. In contrast, 15% (8/55) and 22% (4/18) dense cores have $\alpha \leq 2$ in Ophiuchus and Orion B North respectively. Many of the aforementioned cores that are found to be bounded are also starless in nature. The low ratio of Class 0+I to Class II YSOs in Chamaeleon I, as presented in Dunham et al. (2015), indicates a decelerating rate of star formation as compared to many other nearby star-forming regions, and along with a lack of bound cores, could explain the lack of detections of starless core substructure seen in Dunham et al. (2016).

In Ophiuchus, Kerr et al. (2019) found that the majority of dense cores were found to be unbounded when only considering self-gravity and thermal and non-thermal motions. Only 7% of such cores (5/74) had $\alpha \leq 2$ in the Ophiuchus region (Kerr et al. 2019), presenting a slightly lower percentage of cores compared to this study's 15%. Due to the different dust-based core catalogs used for the analysis, identical results are not expected.

In summary, due to the characteristically different results between the Chamaeleon I cloud and the others clouds in this study, we conduct a broader look at further physical mechanisms through additional virial terms.

6.4. *Virial Analysis*

A number of recent studies implement a more complete virial analysis, often case in terms of energy densities, to gain a fuller picture of the core boundedness (Pattle et al. 2015; Keown et al. 2017; Kirk et al. 2017b; Kerr et al. 2019). Similar to previous studies, we incorporate both the external pressure contributions from the weight of the surrounding molecular cloud, as well as the pressure from the surrounding turbulent medium, but lack uniform data for the contributions of magnetic fields (as introduced in Section 6).

Following the method outlined in Pattle et al. (2015), we describe the contributions given by internal motions

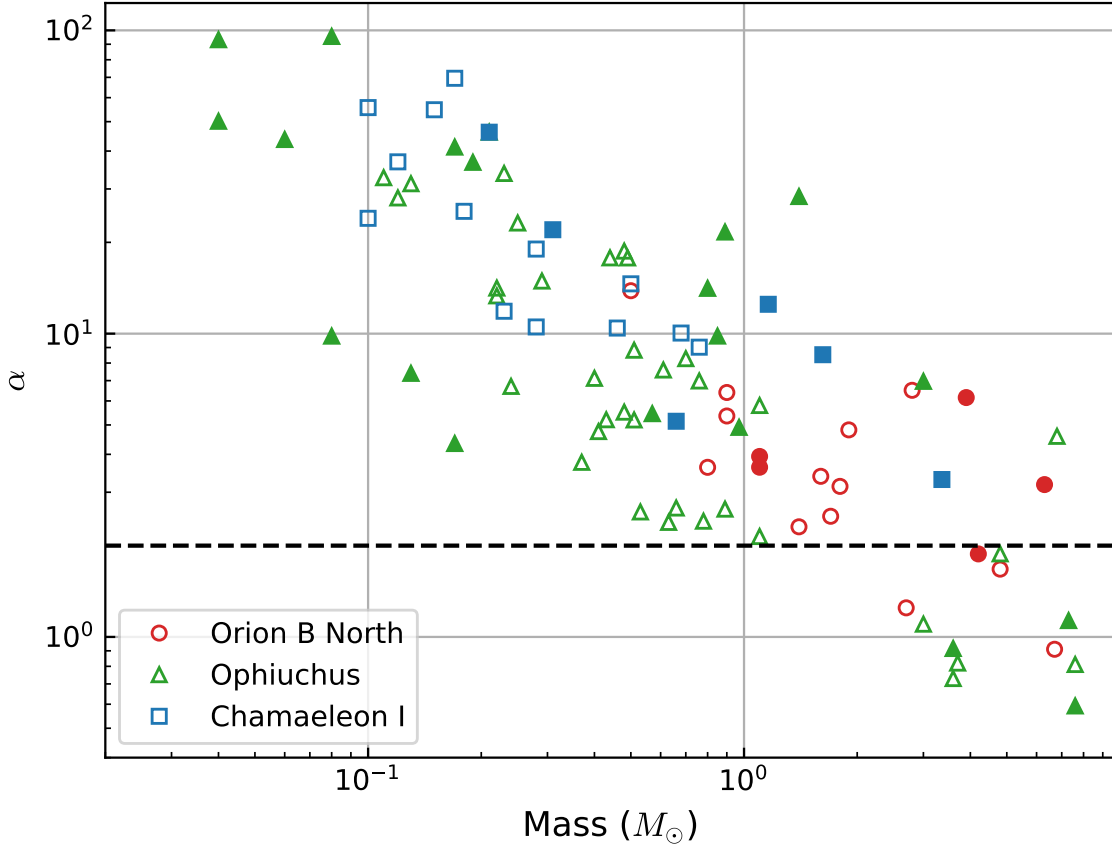


Figure 11. Virial parameter versus core mass, computed for each of the three cloud dense core populations. Each color represents a distinct star forming region. Open markers show the *starless* core population, while filled markers show cores that are protostellar in nature. Cores lying above the dashed line are considered gravitationally unbound.

and self-gravity in the core, as well as the external pressure contributions from the surrounding cloud as the following:

$$\Omega_k = \frac{3}{2} M \sigma_{\text{tot}}^2, \quad (9)$$

$$\Omega_g = -\frac{3}{5} \frac{GM^2}{R}, \quad (10)$$

$$\Omega_P = -4\pi P R^3. \quad (11)$$

We follow [Kerr et al. \(2019\)](#) and choose a constant factor of $-3/5$ for Equation 10, appropriate for sources with constant density, which is a better approximation for cores following the typical $\rho \propto r^{-1}$ density profile.

The contribution of the molecular cloud weight is computed with the following ([McKee 1989](#); [Kirk et al. 2017b](#)):

$$P_w = \pi G \Sigma \bar{\Sigma}, \quad (12)$$

where Σ is the surface mass density along the line-of-sight of the dense core, and $\bar{\Sigma}$ is the mean mass surface

density across the entire cloud. This formulation assumes that the large scale structure is spherically symmetric, with a density falloff following $\rho \propto r^{-1}$; the effect of different geometries is discussed in [Kirk et al. \(2017b\)](#). We compute the mean mass surface density using all pixels above $A_v = 3$ mag associated with the cloud. We convert the extinction into column density using a conversion of $1 \text{ mag} = 9.4 \times 10^{20} \text{ cm}^{-2}$ from [Bohlin et al. \(1978\)](#). The mean extinctions are similar across all three clouds, with values of 4.95 mag, 5.23 mag, and 4.91 mag, for Chamaeleon I, Ophiuchus, and Orion B North respectively. Due to the use of comparatively lower resolution data, the contribution of core material to the extinction measurement is minimal, and further processing of the extinction maps are not required.

To incorporate the contribution from large-scale turbulent pressure, we calculate the line widths of the all-sky CO data (see Section 6.1.3) at the position of each core. We utilize a single component Gaussian model, which is a reasonable representation based on visual checks of the spectra. Assuming the turbulent pressure

to be isotropic in nature, we use the following expression:

$$P_t = n_{\text{CO}} \mu_{\text{mn}} m_{\text{H}} \sigma_{\text{tot,CO}}^2, \quad (13)$$

where the density of the gas that the ^{12}CO lines are probing is given by n_{CO} , and the fitted linewidth is

given by $\sigma_{\text{tot,CO}}$. Due to the lower angular resolution of the ^{12}CO data (0.25 degrees), we utilize the mean density found in star forming cloud environments, 250 cm^{-3} (Bergin & Tafalla 2007) to represent the density of the gas that the ^{12}CO data is probing.

Table 5. Virial Analysis - Starless Core Properties

Core Name ^a	Mass ^a	R_{eff} ^a	T_k ^b	σ_{obs} ^b	Ω_{k} ^c	$-\Omega_{\text{g}}$ ^c	$-\Omega_{\text{P,w}}$ ^c	$-\Omega_{\text{P,t}}$ ^c	Virial ^d
	(M_{\odot})	(pc)	(K)	(km s^{-1})	(erg)	(erg)	(erg)	(erg)	Ratio
Chamaeleon I									
Cha1-C1	3.36	0.035	10.0	0.490	2.71e+43	1.64e+43	4.37e+41	1.33e+42	3.35e-01
Cha1-C2	1.62	0.046	10.0	0.480	1.26e+43	2.95e+42	8.79e+41	2.86e+42	2.66e-01
Cha1-C3	1.16	0.040	10.0	0.530	1.08e+43	1.72e+42	6.82e+41	1.94e+42	2.02e-01
Cha1-C4	0.66	0.035	10.0	0.230	1.63e+42	6.35e+41	4.51e+41	1.55e+42	8.08e-01
Cha1-C8	0.15	0.019	10.0	0.580	1.64e+42	5.99e+40	7.57e+40	2.16e+41	1.07e-01
Cha1-C9	0.68	0.044	10.0	0.320	2.68e+42	5.35e+41	4.47e+41	2.28e+42	6.07e-01
Cha1-C10	0.31	0.032	10.0	0.390	1.68e+42	1.53e+41	3.17e+41	1.01e+42	4.40e-01
Cha1-C11	0.76	0.052	10.0	0.290	2.59e+42	5.73e+41	1.34e+42	4.69e+42	1.28e+00
Cha1-C14	0.21	0.028	10.0	0.520	1.88e+42	8.15e+40	2.37e+41	6.45e+41	2.56e-01
Cha1-C19	0.28	0.036	10.0	0.310	1.05e+42	1.11e+41	5.64e+41	1.49e+42	1.03e+00
Cha1-C21	0.10	0.022	10.0	0.250	2.76e+41	2.30e+40	1.19e+41	3.46e+41	8.84e-01
Cha1-C29	0.17	0.029	10.0	0.570	1.80e+42	5.18e+40	2.15e+41	7.08e+41	2.71e-01
Cha1-C30	0.46	0.050	10.0	0.230	1.14e+42	2.18e+41	9.21e+41	4.19e+42	2.34e+00
Cha1-C31	0.28	0.038	10.0	0.190	5.52e+41	1.05e+41	4.87e+41	1.91e+42	2.27e+00
Cha1-C33	0.18	0.031	10.0	0.310	6.77e+41	5.35e+40	3.02e+41	1.02e+42	1.01e+00
Cha1-C34	0.50	0.052	10.0	0.300	1.79e+42	2.45e+41	8.44e+41	3.30e+42	1.23e+00
Cha1-C35	0.12	0.026	10.0	0.340	5.21e+41	2.83e+40	2.93e+41	7.07e+41	9.87e-01
Cha1-C40	0.23	0.035	10.0	0.190	4.53e+41	7.65e+40	5.30e+41	1.59e+42	2.42e+00
Cha1-C42	0.10	0.024	10.0	0.410	5.91e+41	2.12e+40	1.55e+41	4.25e+41	5.09e-01
Ophiuchus									
162608-24202	0.76	0.028	13.0	0.355	3.74e+42	1.07e+42	5.25e+41	5.42e+41	2.86e-01
162610-24195	0.48	0.023	13.0	0.551	4.91e+42	5.24e+41	2.78e+41	2.94e+41	1.12e-01
162610-24231	0.44	0.023	13.0	0.509	3.92e+42	4.41e+41	2.85e+41	2.94e+41	1.30e-01
162610-24206	0.80	0.032	13.0	0.514	7.24e+42	1.03e+42	8.34e+41	8.42e+41	1.87e-01
162614-24232	0.13	0.012	13.0	0.493	1.09e+42	7.01e+40	5.35e+40	4.85e+40	7.87e-02
162614-24234	0.25	0.018	13.0	0.485	2.04e+42	1.76e+41	1.58e+41	1.54e+41	1.20e-01
162614-24250	1.40	0.039	13.0	0.920	3.69e+43	2.61e+42	1.69e+42	1.47e+42	7.80e-02
162615-24231	0.49	0.025	13.0	0.514	4.43e+42	4.98e+41	4.28e+41	3.88e+41	1.49e-01
162616-24235	0.23	0.017	13.0	0.586	2.62e+42	1.56e+41	1.62e+41	1.37e+41	8.66e-02
162617-24235	0.89	0.031	13.0	0.709	1.44e+43	1.33e+42	8.92e+41	7.32e+41	1.03e-01
162622-24225	3.00	0.042	13.0	0.622	3.81e+43	1.09e+43	1.98e+42	1.93e+42	1.95e-01
162624-24162	0.06	0.007	13.0	0.520	5.54e+41	2.54e+40	8.21e+39	1.30e+40	4.21e-02
162626-24243	7.30	0.048	18.3	0.305	3.22e+43	5.70e+43	3.44e+42	2.84e+42	9.81e-01
162627-24233	3.00	0.023	18.3	0.259	1.09e+43	1.98e+43	3.34e+41	3.24e+41	9.38e-01
162628-24235	7.60	0.043	18.5	0.261	2.80e+43	6.91e+43	2.46e+42	2.03e+42	1.31e+00
162628-24225	4.80	0.051	18.1	0.313	2.18e+43	2.32e+43	3.50e+42	3.39e+42	6.90e-01
162633-24261	6.80	0.073	13.0	0.574	7.48e+43	3.26e+43	1.23e+43	9.65e+42	3.64e-01
162641-24272	0.85	0.033	13.0	0.425	5.56e+42	1.13e+42	1.21e+42	8.79e+41	2.90e-01
162644-24173	0.22	0.015	13.0	0.367	1.14e+42	1.71e+41	7.99e+40	1.04e+41	1.56e-01
162644-24345	0.04	0.007	13.0	0.445	2.83e+41	1.13e+40	9.72e+39	9.65e+39	5.42e-02

Table 5 continued

Table 5 (continued)

Core Name ^a	Mass ^a	R_{eff} ^a	T_k ^b	σ_{obs} ^b	Ω_k ^c	$-\Omega_g$ ^c	$-\Omega_{P,w}$ ^c	$-\Omega_{P,t}$ ^c	Virial ^d
	(M_{\odot})	(pc)	(K)	(km s^{-1})	(erg)	(erg)	(erg)	(erg)	Ratio
162644-24253	0.41	0.023	14.8	0.173	9.09e+41	3.83e+41	3.69e+41	2.87e+41	5.71e-01
162646-24242	0.40	0.022	13.0	0.271	1.34e+42	3.76e+41	3.44e+41	2.60e+41	3.66e-01
162648-24236	0.51	0.026	13.0	0.330	2.25e+42	5.10e+41	5.95e+41	9.04e+41	4.47e-01
162660-24343	3.60	0.053	10.3	0.109	4.57e+42	1.25e+43	4.30e+42	3.75e+42	2.25e+00
162705-24363	0.08	0.010	13.0	0.779	1.54e+42	3.23e+40	2.60e+40	2.65e+40	2.75e-02
162705-24391	0.53	0.023	11.4	0.128	8.00e+41	6.19e+41	2.79e+41	3.16e+41	7.59e-01
162707-24381	0.04	0.007	13.0	0.634	5.26e+41	1.13e+40	8.51e+39	9.65e+39	2.80e-02
162709-24372	0.19	0.015	13.0	0.611	2.34e+42	1.27e+41	6.80e+40	7.72e+40	5.83e-02
162711-24393	0.21	0.017	13.0	0.678	3.12e+42	1.35e+41	1.15e+41	1.18e+41	5.90e-02
162712-24290	0.11	0.012	15.2	0.469	8.72e+41	5.34e+40	5.13e+40	3.95e+40	8.27e-02
162712-24380	0.12	0.013	13.0	0.427	7.91e+41	5.64e+40	5.68e+40	5.63e+40	1.07e-01
162713-24295	0.29	0.017	15.6	0.408	1.84e+42	2.47e+41	1.61e+41	1.33e+41	1.47e-01
162715-24303	0.22	0.017	15.3	0.338	1.05e+42	1.48e+41	1.27e+41	1.17e+41	1.87e-01
162725-24273	0.70	0.023	13.4	0.425	4.61e+42	1.12e+42	3.03e+41	5.77e+41	2.16e-01
162727-24405	3.60	0.055	12.2	0.121	5.51e+42	1.20e+43	3.67e+42	4.24e+42	1.81e+00
162728-24271	0.97	0.022	13.3	0.384	5.43e+42	2.21e+42	2.74e+41	5.23e+41	2.77e-01
162728-24393	0.17	0.015	13.0	0.613	2.10e+42	1.02e+41	7.58e+40	7.73e+40	6.07e-02
162729-24274	0.57	0.023	13.0	0.282	2.01e+42	7.40e+41	2.83e+41	5.77e+41	3.97e-01
162730-24264	0.51	0.019	13.7	0.282	1.83e+42	7.06e+41	1.70e+41	3.41e+41	3.32e-01
162730-24415	0.61	0.029	13.0	0.313	2.49e+42	6.56e+41	5.58e+41	6.19e+41	3.68e-01
162733-24262	1.10	0.028	14.1	0.395	6.51e+42	2.25e+42	5.20e+41	1.06e+42	2.94e-01
162739-24424	0.37	0.023	11.8	0.133	5.87e+41	3.12e+41	2.61e+41	2.88e+41	7.34e-01
162740-24431	0.13	0.013	13.0	0.156	2.45e+41	6.62e+40	5.12e+40	5.64e+40	3.55e-01
162759-24334	0.63	0.025	11.0	0.134	9.55e+41	8.00e+41	3.57e+41	6.90e+41	9.68e-01
162821-24362	0.17	0.014	11.5	0.108	2.33e+41	1.07e+41	5.33e+40	1.10e+41	5.82e-01
163138-24495	1.10	0.031	12.2	0.173	2.18e+42	2.03e+42	3.79e+41	5.74e+41	6.85e-01
163139-24506	0.48	0.026	12.7	0.221	1.24e+42	4.52e+41	2.53e+41	3.62e+41	4.29e-01
163140-24485	0.24	0.018	9.9	0.215	5.45e+41	1.63e+41	8.09e+40	1.21e+41	3.35e-01
163141-24495	0.89	0.029	12.2	0.182	1.84e+42	1.40e+42	3.79e+41	4.96e+41	6.16e-01
163154-24560	0.43	0.023	11.7	0.218	1.06e+42	4.08e+41	1.87e+41	2.54e+41	4.00e-01
163157-24572	0.78	0.031	11.1	0.136	1.20e+42	9.98e+41	3.87e+41	6.63e+41	8.53e-01
163201-24564	0.08	0.009	13.9	0.189	1.85e+41	3.76e+40	9.39e+39	1.44e+40	1.66e-01
163223-24284	7.60	0.041	13.8	0.231	2.15e+43	7.28e+43	1.44e+42	1.68e+42	1.76e+00
163229-24291	3.70	0.047	12.1	0.141	6.19e+42	1.51e+43	2.22e+42	2.50e+42	1.60e+00
163448-24381	0.66	0.031	8.8	0.152	9.74e+41	7.32e+41	3.45e+41	3.06e+41	7.10e-01
Orion B North									
BN-546074-01342	6.30	0.068	17.1	0.449	4.75e+43	2.99e+43	3.57e+42	1.45e+43	5.04e-01
BN-546097-00552	0.50	0.035	15.0	0.353	2.53e+42	3.65e+41	5.42e+41	1.98e+42	5.70e-01
BN-546135-00525	1.10	0.045	12.8	0.213	2.75e+42	1.40e+42	1.32e+42	4.02e+42	1.23e+00
BN-546310-00234	4.20	0.053	16.1	0.284	1.61e+43	1.72e+43	2.34e+42	6.66e+42	8.11e-01
BN-546433-00148	0.80	0.049	12.3	0.119	1.22e+42	6.72e+41	1.31e+42	5.61e+42	3.11e+00
BN-546280-00145	1.90	0.043	13.7	0.379	1.05e+43	4.34e+42	1.44e+42	3.54e+42	4.45e-01
BN-546276-00057	3.90	0.047	15.5	0.630	5.16e+43	1.68e+43	1.96e+42	4.60e+42	2.26e-01
BN-546321-00044	0.90	0.035	12.8	0.320	3.78e+42	1.18e+42	8.10e+41	1.99e+42	5.26e-01
BN-546532-00018	4.80	0.070	16.7	0.221	1.41e+43	1.69e+43	3.42e+42	1.65e+43	1.30e+00
BN-546334-00006	1.10	0.038	15.4	0.210	2.95e+42	1.63e+42	8.09e+41	2.52e+42	8.40e-01
BN-546244-00001	2.80	0.059	15.0	0.470	2.22e+43	6.83e+42	3.87e+42	1.11e+43	4.90e-01
BN-546450+00021	1.70	0.036	16.0	0.234	5.22e+42	4.17e+42	5.08e+41	2.16e+42	6.56e-01
BN-546350+00029	1.60	0.044	17.0	0.235	5.06e+42	2.99e+42	1.17e+42	4.61e+42	8.66e-01
BN-546405+00032	2.70	0.042	15.4	0.153	5.60e+42	8.99e+42	8.17e+41	3.47e+42	1.18e+00
BN-546267+00101	1.80	0.045	13.6	0.259	5.77e+42	3.68e+42	1.32e+42	5.00e+42	8.65e-01
BN-546275+00135	1.40	0.038	13.1	0.183	3.04e+42	2.64e+42	7.93e+41	3.00e+42	1.06e+00

Table 5 continued

Table 5 (continued)

Core Name ^a	Mass ^a	R_{eff} ^a	T_k ^b	σ_{obs} ^b	Ω_k ^c	$-\Omega_g$ ^c	$-\Omega_{P,w}$ ^c	$-\Omega_{P,t}$ ^c	Virial ^d
	(M_{\odot})	(pc)	(K)	(km s^{-1})	(erg)	(erg)	(erg)	(erg)	Ratio
BN-546499+00204	6.70	0.068	17.7	0.155	1.54e+43	3.38e+43	3.05e+42	1.53e+43	1.69e+00
BN-546362+00550	0.90	0.035	15.0	0.270	3.16e+42	1.18e+42	7.36e+41	2.87e+42	7.57e-01

^aDense core name, mass, and effective radius as adopted from Belloche et al. (2011); Jørgensen et al. (2008); Nutter & Ward-Thompson (2007) for Chamaeleon I, Ophiuchus, and Orion B North respectively.

^bObserved linewidth and kinetic temperature as measured from the GAS kinematic dataset. We assume a temperature of $T = 13$ K and $T = 15$ K for Ophiuchus and Orion B North respectively, for all cores which only have linewidth measurements (see Section 6.2 for discussions).

^cVirial parameters as derived in Section 6.4.

^dIndicates whether the dense core is bound taking into account all known virial terms; $-(\Omega_g + \Omega_{P,t} + \Omega_{P,w})/2\Omega_k$.

Our virial results are presented in Table 5, for the total 92 dense cores across the three star forming regions. A dense core is defined as being in a state of virial equilibrium when $2\Omega_k = -(\Omega_g + \Omega_{P,t} + \Omega_{P,w})$. If the virial ratio (as given in the final column of Table 5) is greater than one, a core will be bounded, while a ratio less than one indicates that the core is unbounded and most likely will disperse over time. Figure 12 shows the confinement ratio on the vertical axis, describing the relative contributions of both external pressure and self-gravity, as a function of the virial ratio.

The addition of the contributions of the external pressure terms, do generally shift more cores into the bound regime, as compared to our results from the Jeans analysis. The relative contribution of external pressure indicates that the overall cloud pressure is responsible for much more of the binding in Chamaeleon I cores, up to an order of magnitude on average compared with those found in the Ophiuchus region. Similar to Tsitali et al. (2015), we find Cha1-C1 (also known as Cha-MMS1) to be gravitationally dominated, the only core in our analysis in this domain. Cha-MMS1 is a first hydrostatic core candidate (Belloche et al. 2006, 2011; Tsitali et al. 2013), explaining the much larger contribution of the gravitational virial term in comparison its external pressure term.

With the addition of turbulent and cloud weight pressures, 54% (7/13) of starless cores in Chamaeleon I, 8% (3/36) of starless cores in Ophiuchus, and 38% (5/13) of cores in Orion B North qualify as bound. Compared to the results from Kerr et al. (2019), in which 36% of the cores were found to become bound under the use of all virial terms, we find a lower amount of cores in Ophiuchus that are classified as bound. We do show that most cores in Ophiuchus have more equal contributions

from the two pressure sources, similar to the results from Kerr et al. (2019).

The all-sky CO survey dataset from Dame & Thaddeus (2022) used in this analysis is chosen for its comparable observations and spectral resolution across the entire northern sky (see Section 6.1.3). The individual all-sky CO survey datasets for Chamaeleon (Boulanger et al. 1998), Ophiuchus (de Geus et al. 1990), and Orion (Wilson et al. 2005) do give a higher angular resolution for the Orion and Chamaeleon regions (0.125 degrees), and a higher spectral resolution for Ophiuchus (0.26 km s^{-1}). Utilizing these individual surveys in place of our chosen CO dataset yielded differences in the fitted linewidths of approximately 20% on average, and no more than 30% in difference. These specific changes in the fitted spectra do not significantly change the results shown. In summary, due to the coarse spectral resolution of the surveys (as compared to other similar studies), we are likely to have over-estimated our turbulent pressures across all three core populations.

For typical Milky Way cloud conditions numerical simulations of magnetized, turbulent clouds suggest that ~ 20 -40% of dense cores disperse before forming stars (Smullen et al. 2020; Offner et al. 2022). Low-surface density, less massive clouds like Chamaeleon likely have higher fractions of dispersing starless cores. However, the measured virial parameter, as defined in Equation 5, poorly correlates with whether a given core will go on to collapse. Offner et al. (2022) analyze the relationship between a variety of core properties and their evolution and find that individual statistics, like virial parameter, are poor predictors of whether cores eventually become protostellar. This is perhaps not surprising as observational estimates of boundedness neglect important dynamical indicators, including time variation and the magnetic energy (Dib et al. 2007). However, a more holistic view of core properties, including their degree of velocity coherence, mass, size, and density/velocity

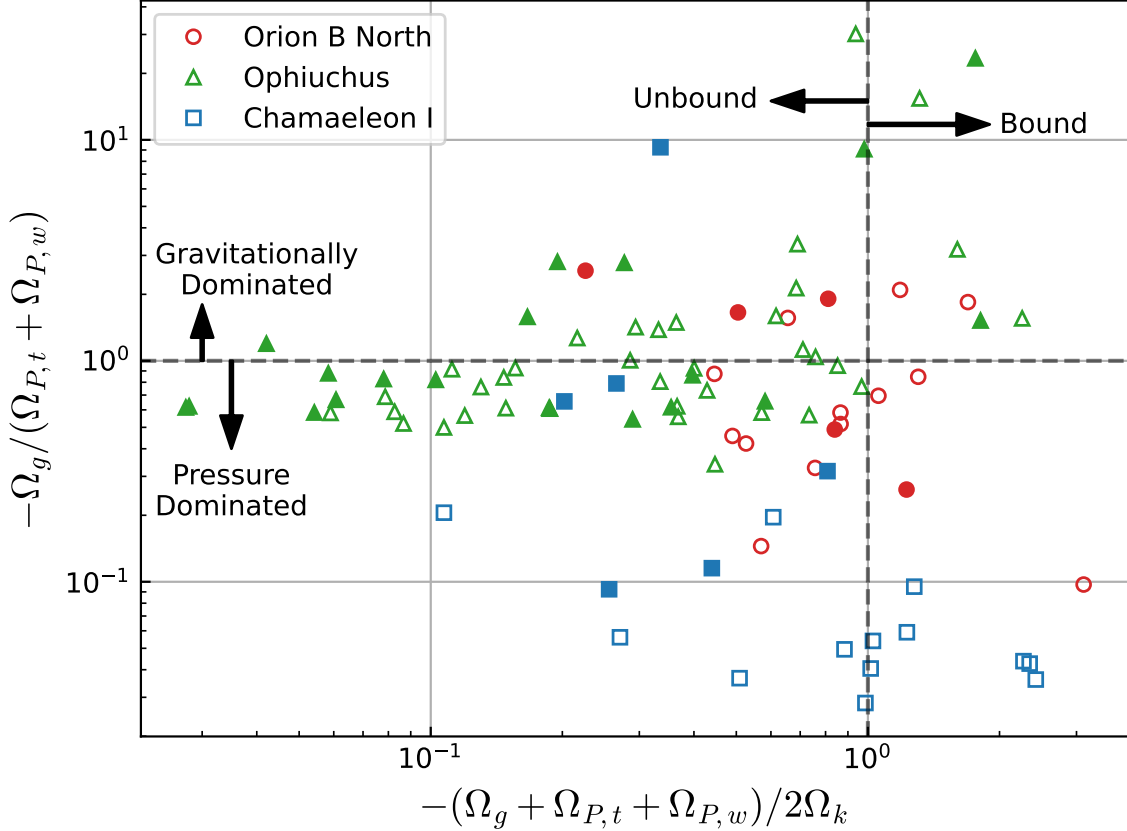


Figure 12. Confinement ratio versus the virial ratio, as computed for each of the three cloud dense core populations. See Figure 11 for plotting conventions. Cores lying above the horizontal dashed line are considered gravitationally dominated, while cores under the dashed line are considered pressure dominated. Cores lying to the right hand side of the vertical dashed line are bounded given the full virial equation used for this study.

profiles, enables more accurate predictions of core outcomes. By mapping core properties inferred from NH_3 observations to those of simulated cores, [Offner et al. \(2022\)](#) predict that at least $58 \pm 14\%$ and $55 \pm 12\%$ of Ophiuchus and Orion cores, respectively, go on to form stars. This suggests that predictions for detectable core substructure that posit 100% of observed cores collapse, as assumed here, are reasonable approximations for these regions.

In summary, while the virial measures of each core may be a poor indicator of its future state, the large difference in bulk population properties between Chamaeleon I and Ophiuchus/Orion B North may lend a plausible explanation for the lack of ALMA detections in the Chamaeleon I region.

7. CONCLUSIONS

In this paper, we present ALMA Cycle 3 Band 3 observations of 73 dense cores in the Orion B North region. We perform synthetic observations of starless core evolution simulations to predict the expected number of starless core detections in our dataset under the tur-

bulent fragmentation model. We summarize our main results as follows:

1. We detect 34 continuum sources across 19 individual ALMA pointings. Four of these detections are most likely starless, as we find no protostellar association nor signs of CO outflow at their location.
2. The likely starless cores detected through our ALMA observations are among the faintest objects in our survey and all are associated with mid- to high-concentration parent cores, as measured by the lower-resolution [NWT07](#) SCUBA data.
3. We generate synthetic observations of isolated starless core evolution simulations to predict the number of starless core detections expected under the turbulent fragmentation model. Out of the 58 truly starless cores observed with ALMA, our one starless core detection agrees with the predicted number of detections 2 ± 1 under the turbulent fragmentation model.

We put these results in the context of previous ALMA surveys by performing a multi-cloud virial analysis with dense core populations observed with ALMA. The Ophiuchus and Orion B North results are consistent with the turbulent fragmentation picture, while Chamaeleon I results are not. We perform an additional virial analysis on all three dense core populations, and find that Chamaeleon I shows features unlike both Ophiuchus and Orion B North. According to our simple Jeans analysis, no Chamaeleon I cores are bound. With the contributions of external pressure terms in our virial analysis, we show that for the Chamaeleon I cores, an order of magnitude more of the binding energy is attributed to cloud weight and cloud-scale turbulent pressure than self-gravity, compared with the other two clouds. These differences lend weight to the findings of Tsitali et al. (2015), in which the dense cores in Chamaeleon I, unlike the majority of cores in most star-forming regions, are destined to re-expand without forming stars.

ACKNOWLEDGEMENTS

We thank the referee for their insightful and quick reports which improved the manuscript. We acknowledge the helpful input from John Tobin, the external examiner for SF’s MSc thesis, upon which this paper is based. SF acknowledges and respects the Lekwungen-speaking peoples on whose traditional territories SF works and lives, and the Songhees, Esquimalt and WSANEC peoples whose historical relationships with the land continue to this day. The National Radio Astronomy Observatory is a facility of the National Science Foundation operated under cooperative agreement by Associated Universities, Inc. This paper makes use of the following ALMA data, with project code: #2015.1.00094.S. ALMA is a partnership of ESO (representing its member states), NSF (USA), and NINS (Japan), together

with NRC (Canada) and NSC and ASIAA (Taiwan), in cooperation with the Republic of Chile. The Joint ALMA Observatory is operated by ESO, AUI/NRAO, and NAOJ. This research also made use of NASA’s Astrophysics Data System (ADS) Abstract Service. This research has made use of the SIMBAD database, operated at CDS, Strasbourg, France (Wenger et al. 2000). The JCMT has historically been operated by the Joint Astronomy Center on behalf of the Science and Technology Facilities Council of the United Kingdom, the National Research Council of Canada and the Netherlands Organisation for Scientific Research. The authors acknowledge the use of the Canadian Advanced Network for Astronomy Research (CANFAR) Science Platform. Our work used the facilities of the Canadian Astronomy Data Center, operated by the National Research Council of Canada with the support of the Canadian Space Agency, and CANFAR, a consortium that serves the data-intensive storage, access, and processing needs of university groups and centers engaged in astronomy research (Gaudet et al. 2010). We thank the GAS Team for their publicly available DR1 dataset. SF and HK acknowledge support from an NSERC Discovery Grant. SO acknowledges support from NSF Career grant 1748571 and a Moncrief Grant Challenge Award.

DATA AVAILABILITY

All associated data, including compiled figures and tables, are publicly available at the CADC via the following link: <http://doi.org/10.11570/24.0007> (Fielder & Kirk 2024).

Facilities: ALMA, JCMT, GBT

Software: (Astropy Astropy Collaboration et al. 2013, 2018, 2022), (CASA The CASA Team et al. 2022)

APPENDIX

A. COMPARISON OF SCUBA AND SCUBA-2 DATA

While not available at the time of the ALMA proposal, the Orion molecular cloud was observed by the JCMT Gould Belt Survey with the SCUBA-2 instrument (Kirk et al. 2016), which has larger spatial coverage and improved sensitivity compared to the NWT07 SCUBA observations. The SCUBA NWT07 has a sensitivity of 16 mJy beam^{-1} at $850 \mu\text{m}$, while comparatively, the SCUBA-2 observations by Kirk et al. (2016) has a sensitivity of $3.4 \text{ mJy beam}^{-1}$ at the same wavelength. Additionally, two different core finding algorithms were used to identify over-dense structures in the emission maps, leading to slightly different core positions and footprints when looking at the same star forming region. For example, in Figure 5, the two ALMA observations for this paper (derived from the NWT07 catalog) lie approximately in between 3 distinct SCUBA-2 cores, as shown by the light blue contours over-plotted. While we use the SCUBA observations for most of our analysis, the SCUBA-2 cores are mentioned when this context is needed.

According to Kirk et al. (2016), each peak flux position from the SCUBA dataset was associated with the SCUBA-2 core whose boundary it lies within, resulting in all 100 SCUBA cores finding an association with a SCUBA-2 core.

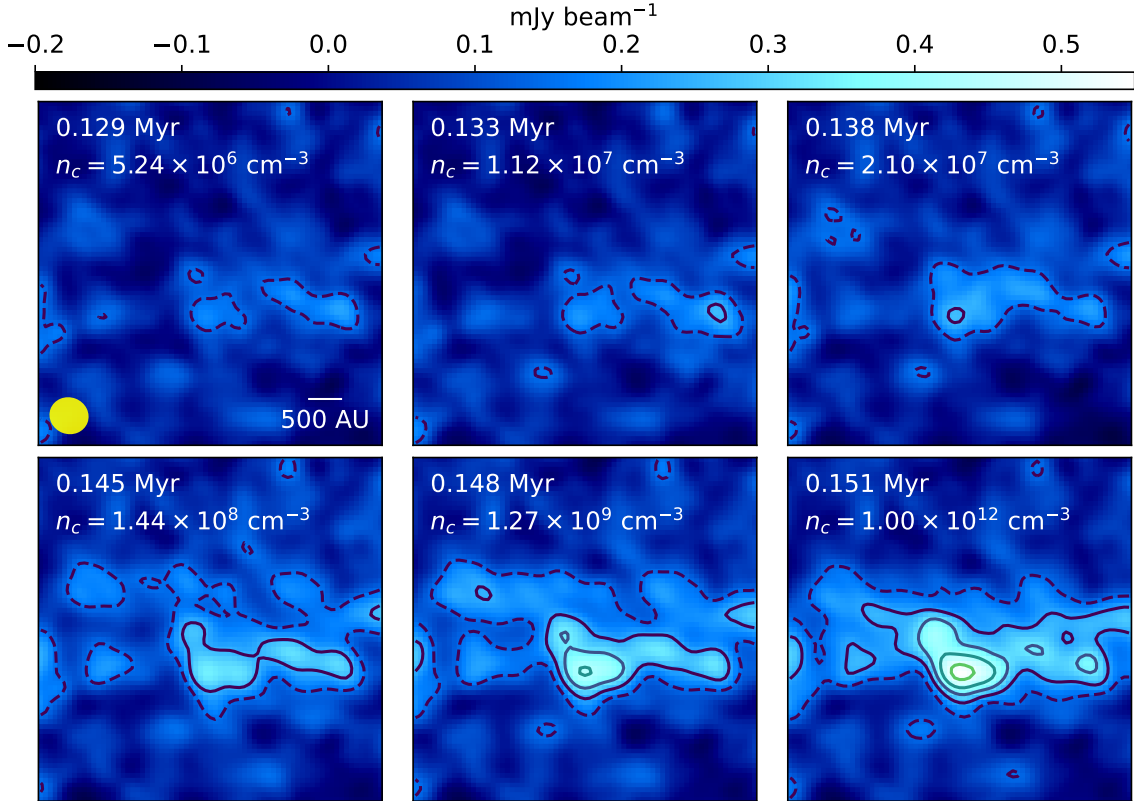


Figure 13. Synthetic ALMA 106 GHz observations of the $4M_{\odot}$ simulation, at six given timesteps, indicated in each panel along side the central density of the core. We adopt the same plotting convention as Figure 8.

Associated core values agree reasonably well between the two datasets, with some scatter present when looking at cores which have one-to-one associations (Kirk et al. 2016). Due to the increased sensitivity of the SCUBA-2 map and the different core-finding algorithm adopted, there is not a one-to-one correspondence between *all* SCUBA and SCUBA-2 cores. In some cases, multiple SCUBA cores map to the same SCUBA-2 core, and in others, a single SCUBA core is subdivided into multiple SCUBA-2 cores.

By comparing both core catalogs, we find six instances where either two or three starless SCUBA cores correspond to a single SCUBA-2 core. In these instances, the multiple peaks identified in the SCUBA map lie along a shared filamentary structure, and the brightest of the SCUBA cores peaks in a similar location to the corresponding SCUBA-2 core peak. Meanwhile, the remaining SCUBA cores lie within the larger elongated footprint of the SCUBA-2 core rather than being associated with unique SCUBA-2 cores. These eight SCUBA cores that do not have unique SCUBA-2 core correspondences are potentially artificially subdivided components of a single larger structure rather than distinct cores. Additionally, we find three instances where individual SCUBA cores were found to lie inside of the associated SCUBA-2 core footprint but with separations between the SCUBA and SCUBA-2 peaks of 50-100 arcsec; we consider these tentatively non-correspondent. Finally, we find one instance where a SCUBA core has no corresponding SCUBA-2 core.

We additionally find three instances where individual SCUBA cores are each subdivided into two SCUBA-2 cores.

Using the SCUBA versus SCUBA-2 comparisons gives a guide to the accuracy and reliability in the cores identified, including their total number. We expect that the true number of distinct cores surveyed lies between the two extremes of the SCUBA and SCUBA-2 core comparisons described here. In summary, there may be as few as 47 or as high as 61 starless cores observed with ALMA.

B. SYNTHETIC OBSERVATIONS OF SIMULATED $4M_{\odot}$ STARLESS CORE EVOLUTION

The starless core population in Orion B North, as catalogued by NWT07, shows a typical mass of $1.4M_{\odot}$. Similar to Dunham et al. (2016), we run synthetic observations on simulation snapshots of a $4M_{\odot}$ starless core and its evolution.

Figure 13 shows that even in the case where the initial mass changes by a factor of 10, the detectability occurs at a similar central density threshold. Dunham et al. (2016) explore a similar set of results, and find that although the initial mass is vastly different between the two simulations, the amount of mass on compact scales, in this case approximately 1000 au, are similar. Additionally, due to the larger distance of 419 pc to the Orion B North cloud compared to Chamaeleon I (140 pc), there is overall less change within the primary beam over consecutive timesteps, leading to such an increase in detectability in the later timesteps shown.

C. FIGURES

Although continuum images were made for all 73 individual fields observed, only a total of 19 individual fields yielded positive detections, of which many have been mosaicked together for better sensitivity. Below, we show all the remaining continuum detections found in our analysis.

REFERENCES

- André, P., Di Francesco, J., Ward-Thompson, D., et al. 2014, *From Filamentary Networks to Dense Cores in Molecular Clouds: Toward a New Paradigm for Star Formation* (eprint: arXiv:1312.6232), 27–51, doi: [10.2458/azu_uapress.9780816531240-ch002](https://doi.org/10.2458/azu_uapress.9780816531240-ch002)
- Astropy Collaboration, Robitaille, T. P., Tollerud, E. J., et al. 2013, *A&A*, 558, A33, doi: [10.1051/0004-6361/201322068](https://doi.org/10.1051/0004-6361/201322068)
- Astropy Collaboration, Price-Whelan, A. M., Sipőcz, B. M., et al. 2018, *AJ*, 156, 123, doi: [10.3847/1538-3881/aabc4f](https://doi.org/10.3847/1538-3881/aabc4f)
- Astropy Collaboration, Price-Whelan, A. M., Lim, P. L., et al. 2022, *ApJ*, 935, 167, doi: [10.3847/1538-4357/ac7c74](https://doi.org/10.3847/1538-4357/ac7c74)
- Ballesteros-Paredes, J., Klessen, R. S., Mac Low, M. M., & Vazquez-Semadeni, E. 2007, *Molecular Cloud Turbulence and Star Formation* (eprint: arXiv:astro-ph/0603357), 63, doi: [10.48550/arXiv.astro-ph/0603357](https://doi.org/10.48550/arXiv.astro-ph/0603357)
- Beichman, C. A., Myers, P. C., Emerson, J. P., et al. 1986, *ApJ*, 307, 337, doi: [10.1086/164421](https://doi.org/10.1086/164421)
- Belloche, A., Parise, B., van der Tak, F. F. S., et al. 2006, *A&A*, 454, L51, doi: [10.1051/0004-6361:20065306](https://doi.org/10.1051/0004-6361:20065306)
- Belloche, A., Schuller, F., Parise, B., et al. 2011, *A&A*, 527, A145, doi: [10.1051/0004-6361/201015733](https://doi.org/10.1051/0004-6361/201015733)
- Bergin, E. A., & Tafalla, M. 2007, *ARA&A*, 45, 339, doi: [10.1146/annurev.astro.45.071206.100404](https://doi.org/10.1146/annurev.astro.45.071206.100404)
- Bertoldi, F., & McKee, C. F. 1992, *ApJ*, 395, 140, doi: [10.1086/171638](https://doi.org/10.1086/171638)
- Bohlin, R. C., Savage, B. D., & Drake, J. F. 1978, *ApJ*, 224, 132, doi: [10.1086/156357](https://doi.org/10.1086/156357)
- Bonnor, W. B. 1956, *MNRAS*, 116, 351, doi: [10.1093/mnras/116.3.351](https://doi.org/10.1093/mnras/116.3.351)
- Boulanger, F., Bronfman, L., Dame, T. M., & Thaddeus, P. 1998, *A&A*, 332, 273
- Caselli, P., Pineda, J. E., Zhao, B., et al. 2019, *ApJ*, 874, 89, doi: [10.3847/1538-4357/ab0700](https://doi.org/10.3847/1538-4357/ab0700)
- Chen, X., Arce, H. G., Zhang, Q., et al. 2013, *ApJ*, 768, 110, doi: [10.1088/0004-637X/768/2/110](https://doi.org/10.1088/0004-637X/768/2/110)
- Dame, T. M., Hartmann, D., & Thaddeus, P. 2001, *ApJ*, 547, 792, doi: [10.1086/318388](https://doi.org/10.1086/318388)
- Dame, T. M., & Thaddeus, P. 2022, *ApJS*, 262, 5, doi: [10.3847/1538-4365/ac7e53](https://doi.org/10.3847/1538-4365/ac7e53)
- Das, I., Basu, S., & André, P. 2021, *Astronomy and Astrophysics*, 649, L13, doi: [10.1051/0004-6361/202140404](https://doi.org/10.1051/0004-6361/202140404)
- de Geus, E. J., Bronfman, L., & Thaddeus, P. 1990, *A&A*, 231, 137
- di Francesco, J., Evans, II, N. J., Caselli, P., et al. 2007, *An Observational Perspective of Low-Mass Dense Cores I: Internal Physical and Chemical Properties* (eprint: arXiv:astro-ph/0602379), 17, doi: [10.48550/arXiv.astro-ph/0602379](https://doi.org/10.48550/arXiv.astro-ph/0602379)
- Dib, S., Kim, J., Vázquez-Semadeni, E., Burkert, A., & Shadmehri, M. 2007, *ApJ*, 661, 262, doi: [10.1086/513708](https://doi.org/10.1086/513708)
- Dunham, M. M., Allen, L. E., Evans, II, N. J., et al. 2015, *ApJS*, 220, 11, doi: [10.1088/0067-0049/220/1/11](https://doi.org/10.1088/0067-0049/220/1/11)
- Dunham, M. M., Offner, S. S. R., Pineda, J. E., et al. 2016, *ApJ*, 823, 160, doi: [10.3847/0004-637X/823/2/160](https://doi.org/10.3847/0004-637X/823/2/160)
- Dutta, S., Lee, C.-F., Liu, T., et al. 2020, *ApJS*, 251, 20, doi: [10.3847/1538-4365/abba26](https://doi.org/10.3847/1538-4365/abba26)
- Ebert, R. 1955, *Zeitschrift für Astrophysik*, 37, 217
- Enoch, M. L., Glenn, J., Evans, II, N. J., et al. 2007, *ApJ*, 666, 982, doi: [10.1086/520321](https://doi.org/10.1086/520321)
- Fang, M., van Boekel, R., Wang, W., et al. 2009, *A&A*, 504, 461, doi: [10.1051/0004-6361/200912468](https://doi.org/10.1051/0004-6361/200912468)
- Federman, S., Megeath, S. T., Tobin, J. J., et al. 2023, *ApJ*, 944, 49, doi: [10.3847/1538-4357/ac9f4b](https://doi.org/10.3847/1538-4357/ac9f4b)
- Fielder, S., & Kirk, H. 2024, *An ALMA Search for Substructure and Fragmentation in Starless Cores in Orion B North, CADC*, doi: [xx.xxxxx/xx.xxxx](https://doi.org/xx.xxxxx/xx.xxxx)
- Fischer, W. J., Megeath, S. T., Ali, B., et al. 2010, *A&A*, 518, L122, doi: [10.1051/0004-6361/201014636](https://doi.org/10.1051/0004-6361/201014636)
- Flaherty, K. M., & Muzerolle, J. 2008, *AJ*, 135, 966, doi: [10.1088/0004-6256/135/3/966](https://doi.org/10.1088/0004-6256/135/3/966)

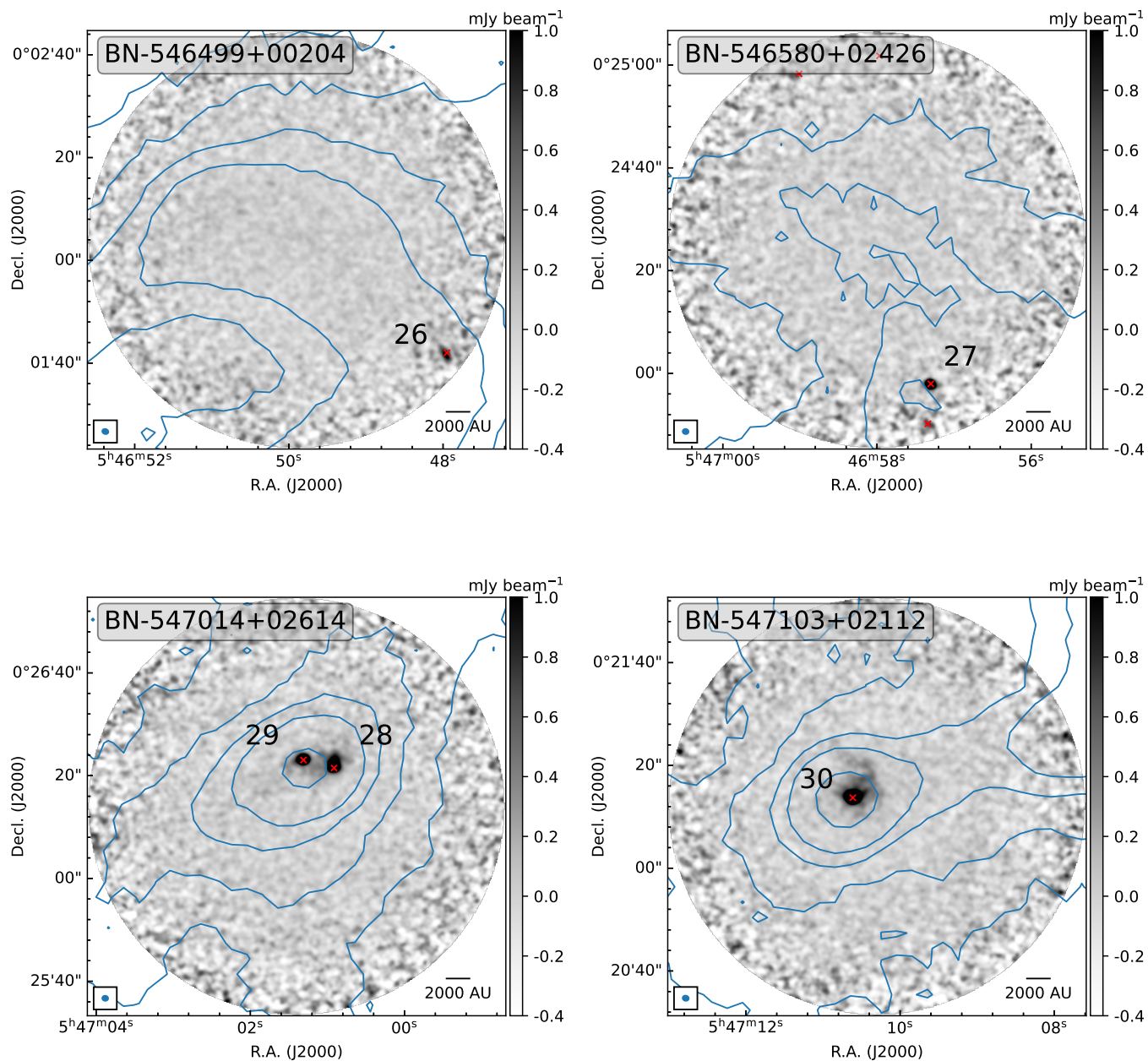


Figure 14. ALMA single pointing fields that harbor detections. See Figure 3 for plotting conventions. All detections in these individual pointings have an associated protostellar association.

Friesen, R. K., Pineda, J. E., co-PIs, et al. 2017, *ApJ*, 843, 63, doi: [10.3847/1538-4357/aa6d58](https://doi.org/10.3847/1538-4357/aa6d58)

Fujishiro, K., Tokuda, K., Tachihara, K., et al. 2020, *ApJL*, 899, L10, doi: [10.3847/2041-8213/ab9ca8](https://doi.org/10.3847/2041-8213/ab9ca8)

Furlan, E., Fischer, W. J., Ali, B., et al. 2016, *ApJS*, 224, 5, doi: [10.3847/0067-0049/224/1/5](https://doi.org/10.3847/0067-0049/224/1/5)

Gaudet, S., Hill, N., Armstrong, P., et al. 2010, in *SPIE Astronomical Telescopes + Instrumentation*, ed. N. M. Radziwill & A. Bridger, San Diego, California, USA, 77401I, doi: [10.1117/12.858026](https://doi.org/10.1117/12.858026)

Girichidis, P., Konstandin, L., Whitworth, A. P., & Klessen, R. S. 2014, *ApJ*, 781, 91, doi: [10.1088/0004-637X/781/2/91](https://doi.org/10.1088/0004-637X/781/2/91)

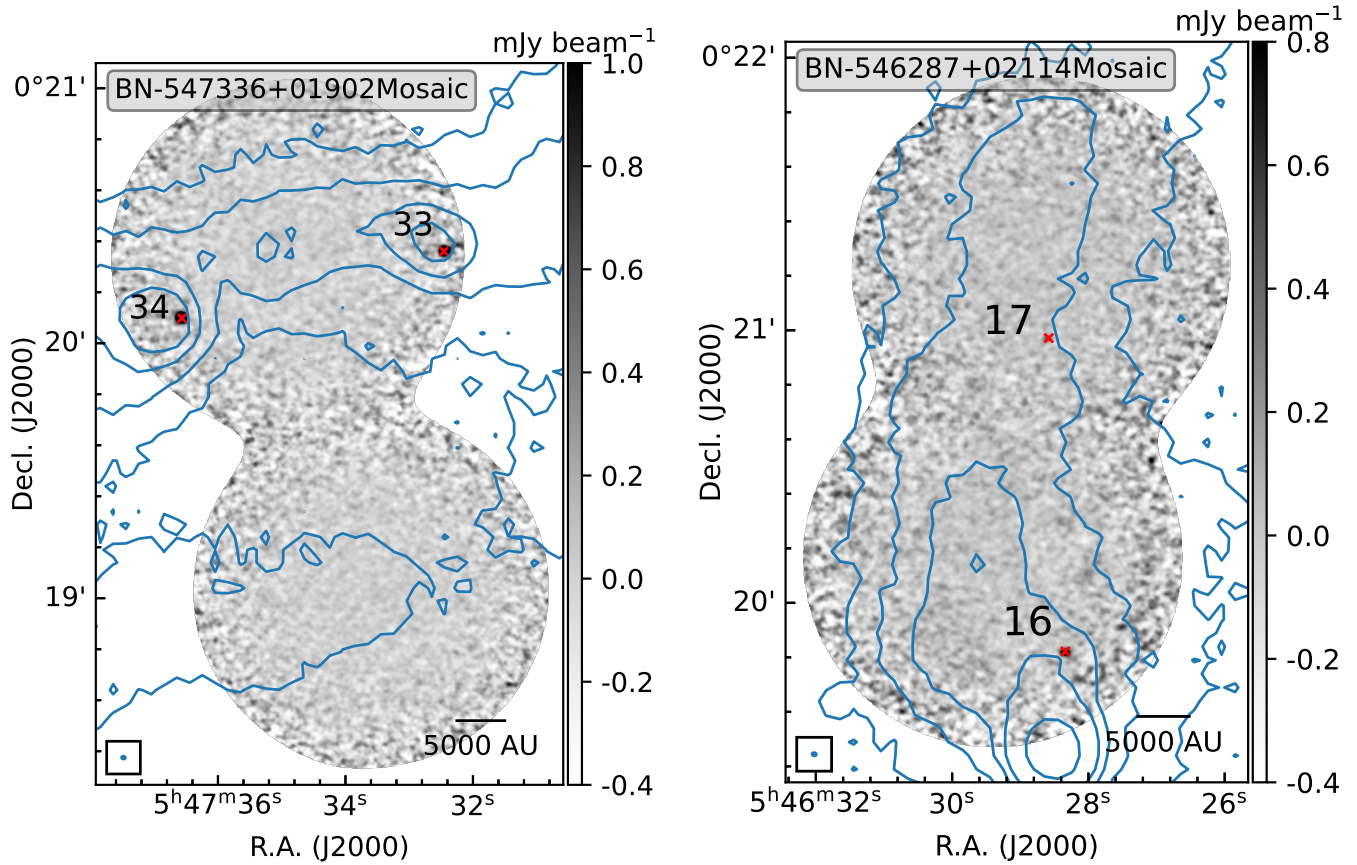


Figure 15. ALMA mosaic fields that harbor detections. See Figure 3 for plotting conventions. All detections in these mosaic pointings have an associated protostellar association.

Goodwin, S. P., Nutter, D., Kroupa, P., Ward-Thompson, D., & Whitworth, A. P. 2008, *A&A*, 477, 823, doi: [10.1051/0004-6361:20078452](https://doi.org/10.1051/0004-6361:20078452)

Hirano, N., Sahu, D., Liu, S.-Y., et al. 2024, *ApJ*, 961, 123, doi: [10.3847/1538-4357/ad09e2](https://doi.org/10.3847/1538-4357/ad09e2)

Holman, K., Walch, S. K., Goodwin, S. P., & Whitworth, A. P. 2013, *MNRAS*, 432, 3534, doi: [10.1093/mnras/stt705](https://doi.org/10.1093/mnras/stt705)

Ikeda, N., Kitamura, Y., & Sunada, K. 2009, *ApJ*, 691, 1560, doi: [10.1088/0004-637X/691/2/1560](https://doi.org/10.1088/0004-637X/691/2/1560)

Jessop, N. E., & Ward-Thompson, D. 2000, *MNRAS*, 311, 63, doi: [10.1046/j.1365-8711.2000.03011.x](https://doi.org/10.1046/j.1365-8711.2000.03011.x)

Jijina, J., Myers, P. C., & Adams, F. C. 1999, *ApJS*, 125, 161, doi: [10.1086/313268](https://doi.org/10.1086/313268)

Johnstone, D., Rosolowsky, E., Tafalla, M., & Kirk, H. 2010, *ApJ*, 711, 655, doi: [10.1088/0004-637X/711/2/655](https://doi.org/10.1088/0004-637X/711/2/655)

Johnstone, D., Wilson, C. D., Moriarty-Schieven, G., et al. 2000, *ApJ*, 545, 327, doi: [10.1086/317790](https://doi.org/10.1086/317790)

Jørgensen, J. K., Johnstone, D., Kirk, H., & Myers, P. C. 2007, *ApJ*, 656, 293, doi: [10.1086/510150](https://doi.org/10.1086/510150)

Jørgensen, J. K., Johnstone, D., Kirk, H., et al. 2008, *ApJ*, 683, 822, doi: [10.1086/589956](https://doi.org/10.1086/589956)

Kauffmann, J., Bertoldi, F., Bourke, T. L., Evans, II, N. J., & Lee, C. W. 2008, *A&A*, 487, 993, doi: [10.1051/0004-6361:200809481](https://doi.org/10.1051/0004-6361:200809481)

Keown, J., Di Francesco, J., Kirk, H., et al. 2017, *ApJ*, 850, 3, doi: [10.3847/1538-4357/aa93ec](https://doi.org/10.3847/1538-4357/aa93ec)

Kerr, R., Kirk, H., Di Francesco, J., et al. 2019, *ApJ*, 874, 147, doi: [10.3847/1538-4357/ab0c08](https://doi.org/10.3847/1538-4357/ab0c08)

Kirk, H., Johnstone, D., & Di Francesco, J. 2006, *ApJ*, 646, 1009, doi: [10.1086/503193](https://doi.org/10.1086/503193)

Kirk, H., Francesco, J. D., Johnstone, D., et al. 2016, *ApJ*, 817, 167, doi: [10.3847/0004-637X/817/2/167](https://doi.org/10.3847/0004-637X/817/2/167)

Kirk, H., Dunham, M. M., Di Francesco, J., et al. 2017a, *ApJ*, 838, 114, doi: [10.3847/1538-4357/aa63f8](https://doi.org/10.3847/1538-4357/aa63f8)

Kirk, H., Friesen, R. K., Pineda, J. E., et al. 2017b, *ApJ*, 846, 144, doi: [10.3847/1538-4357/aa8631](https://doi.org/10.3847/1538-4357/aa8631)

Kirk, J. M., Ward-Thompson, D., & André, P. 2005, *MNRAS*, 360, 1506, doi: [10.1111/j.1365-2966.2005.09145.x](https://doi.org/10.1111/j.1365-2966.2005.09145.x)

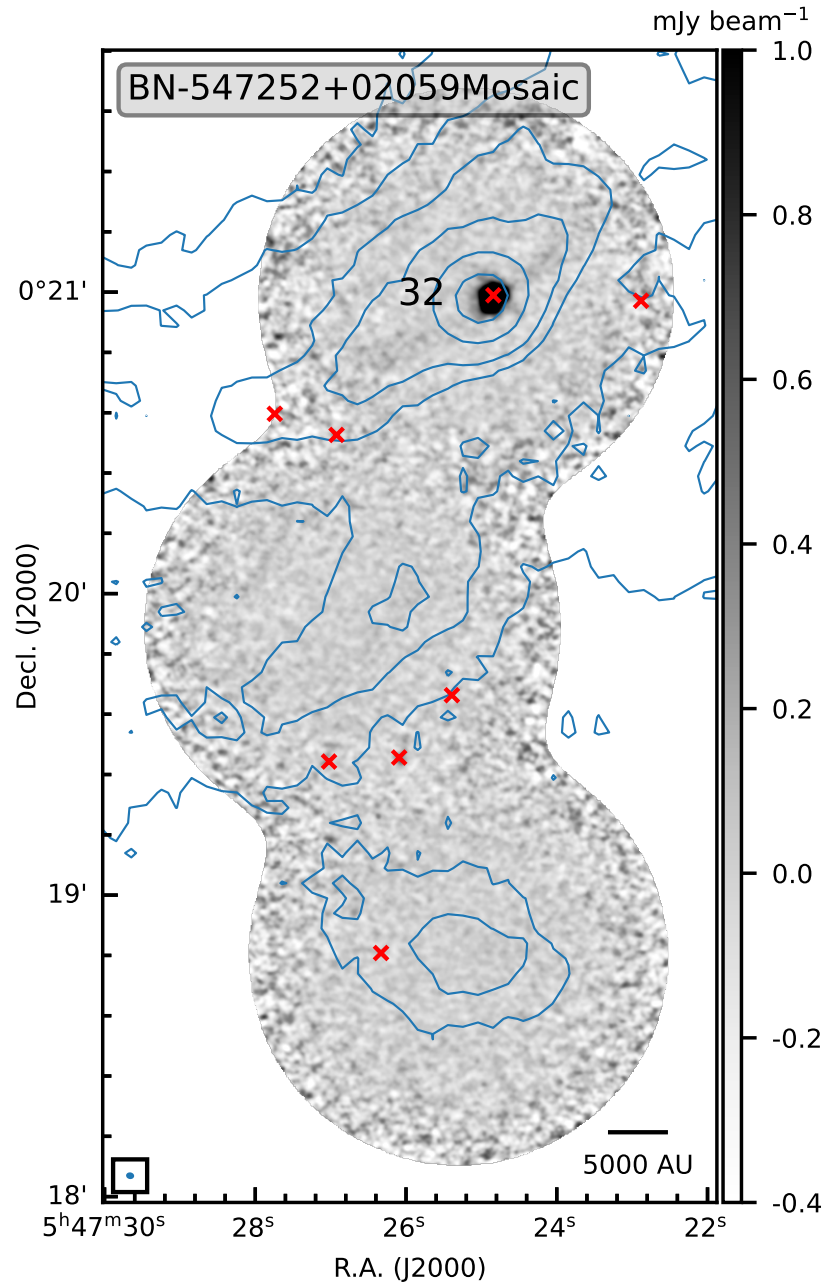


Figure 16. ALMA mosaic field that harbor detections. See Figure 3 for plotting conventions. All detections in this mosaic pointing have an associated protostellar association.

Könyves, V., André, Ph., Men'shchikov, A., et al. 2015,

A&A, 584, A91, doi: [10.1051/0004-6361/201525861](https://doi.org/10.1051/0004-6361/201525861)

Könyves, V., André, Ph., Arzoumanian, D., et al. 2020,

A&A, 635, A34, doi: [10.1051/0004-6361/201834753](https://doi.org/10.1051/0004-6361/201834753)

Kramer, C., Stutzki, J., Rohrig, R., & Corneliussen, U.

1998, A&A, 329, 249

Kuruwita, R. L., & Haugbølle, T. 2023, A&A, 674, A196,

doi: [10.1051/0004-6361/202244882](https://doi.org/10.1051/0004-6361/202244882)

Lee, A. T., Offner, S. S. R., Kratter, K. M., Smullen, R. A.,

& Li, P. S. 2019, ApJ, 887, 232,

doi: [10.3847/1538-4357/ab584b](https://doi.org/10.3847/1538-4357/ab584b)

Li, P., Cunningham, A., Gaches, B., et al. 2021, The

Journal of Open Source Software, 6, 3771,

doi: [10.21105/joss.03771](https://doi.org/10.21105/joss.03771)

Lomax, O., Whitworth, A. P., Hubber, D. A., Stamatellos,

D., & Walch, S. 2015, MNRAS, 447, 1550,

doi: [10.1093/mnras/stu2530](https://doi.org/10.1093/mnras/stu2530)

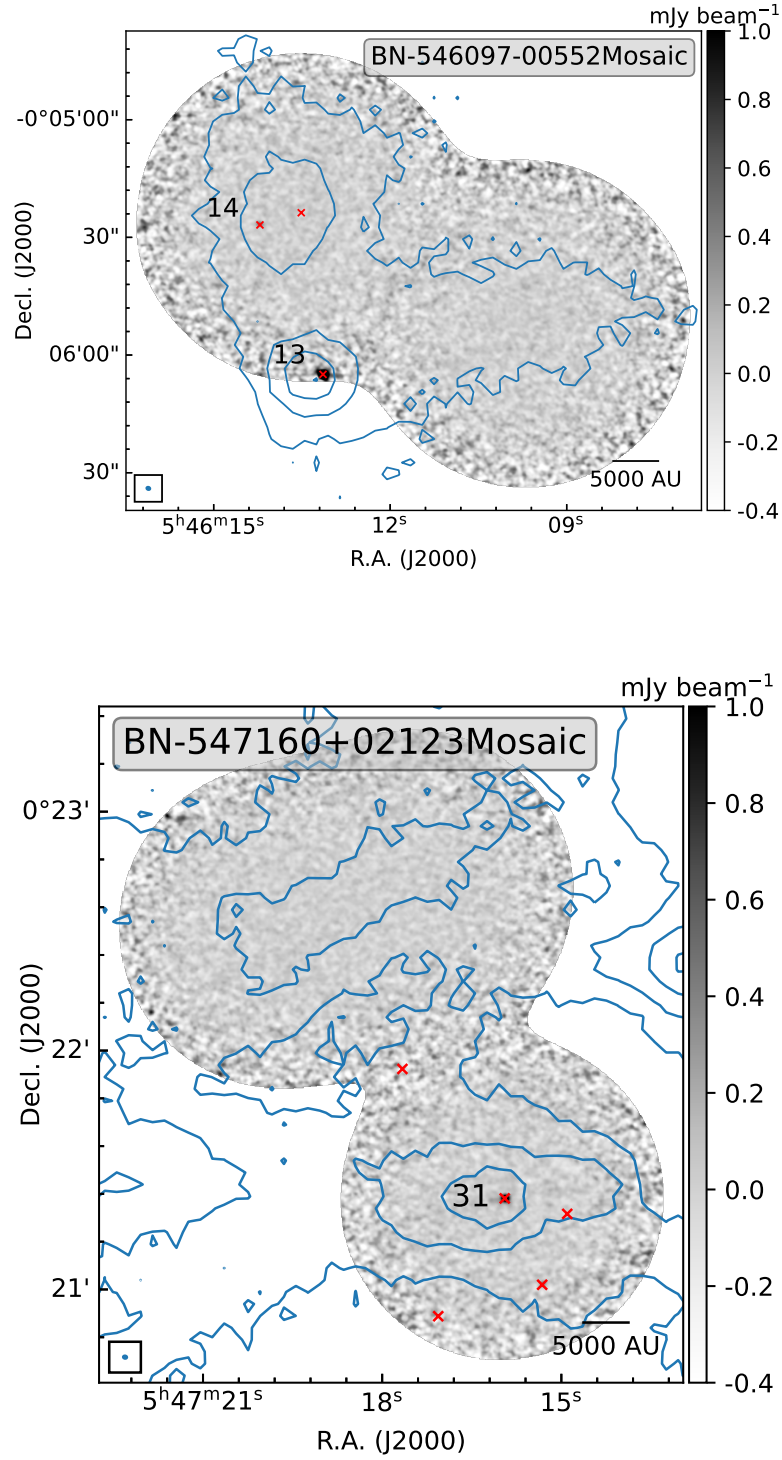


Figure 17. ALMA mosaic fields that harbor detections. See Figure 3 for plotting conventions. All detections in these mosaic pointings have an associated protostellar association.

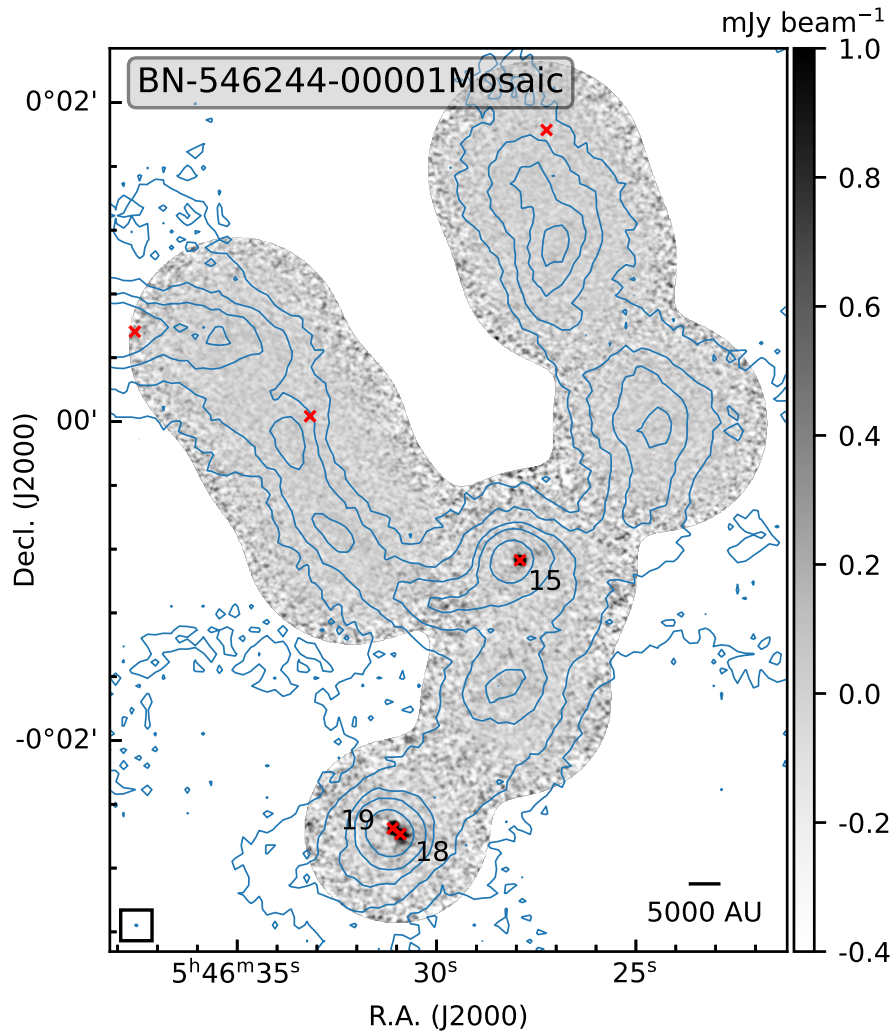


Figure 18. ALMA mosaic field BN-546244-00001 that harbor detections. See Figure 3 for plotting conventions. All detections in this mosaic pointing have an associated protostellar association.

- Luo, Q.-y., Liu, T., Lee, A. T., et al. 2023, *ApJ*, 952, L2, doi: [10.3847/2041-8213/acdddf](https://doi.org/10.3847/2041-8213/acdddf)
- Mac Low, M.-M., & Klessen, R. S. 2004, *Reviews of Modern Physics*, 76, 125, doi: [10.1103/RevModPhys.76.125](https://doi.org/10.1103/RevModPhys.76.125)
- Machida, M. N., Inutsuka, S.-i., & Matsumoto, T. 2008, *ApJ*, 676, 1088, doi: [10.1086/528364](https://doi.org/10.1086/528364)
- Marton, G., Tóth, L. V., Paladini, R., et al. 2016, *MNRAS*, 458, 3479, doi: [10.1093/mnras/stw398](https://doi.org/10.1093/mnras/stw398)
- McKee, C. F. 1989, *ApJ*, 345, 782, doi: [10.1086/167950](https://doi.org/10.1086/167950)
- Megeath, S. T., Gutermuth, R., Muzerolle, J., et al. 2012, *AJ*, 144, 192, doi: [10.1088/0004-6256/144/6/192](https://doi.org/10.1088/0004-6256/144/6/192)
- Moe, M., & Di Stefano, R. 2017, *ApJS*, 230, 15, doi: [10.3847/1538-4365/aa6fb6](https://doi.org/10.3847/1538-4365/aa6fb6)
- Motte, F., Andre, P., & Neri, R. 1998, *A&A*, 336, 150
- Motte, F., Bontemps, S., Schilke, P., et al. 2007, *A&A*, 476, 1243, doi: [10.1051/0004-6361:20077843](https://doi.org/10.1051/0004-6361:20077843)
- Murillo, N. M., Van Dishoeck, E. F., Hacar, A., Harsono, D., & Jørgensen, J. K. 2022, *A&A*, 658, A53, doi: [10.1051/0004-6361/202141250](https://doi.org/10.1051/0004-6361/202141250)
- Nutter, D., & Ward-Thompson, D. 2007, *MNRAS*, 374, 1413, doi: [10.1111/j.1365-2966.2006.11246.x](https://doi.org/10.1111/j.1365-2966.2006.11246.x)
- Offner, S. S. R., Capodilupo, J., Schnee, S., & Goodman, A. A. 2012, *MNRAS*, 420, L53, doi: [10.1111/j.1745-3933.2011.01194.x](https://doi.org/10.1111/j.1745-3933.2011.01194.x)
- Offner, S. S. R., & Chaban, J. 2017, *ApJ*, 847, 104, doi: [10.3847/1538-4357/aa8996](https://doi.org/10.3847/1538-4357/aa8996)
- Offner, S. S. R., Clark, P. C., Hennebelle, P., et al. 2014, *The Origin and Universality of the Stellar Initial Mass Function* (eprint: arXiv:1312.5326), 53–75, doi: [10.2458/azu_uapress.9780816531240-ch003](https://doi.org/10.2458/azu_uapress.9780816531240-ch003)
- Offner, S. S. R., Moe, M., Kratter, K. M., et al. 2023, 534, 275, doi: [10.48550/arXiv.2203.10066](https://doi.org/10.48550/arXiv.2203.10066)
- Offner, S. S. R., Taylor, J., Markey, C., et al. 2022, *MNRAS*, 517, 885, doi: [10.1093/mnras/stac2734](https://doi.org/10.1093/mnras/stac2734)
- Ohashi, S., Sanhueza, P., Sakai, N., et al. 2018, *ApJ*, 856, 147, doi: [10.3847/1538-4357/aab3d0](https://doi.org/10.3847/1538-4357/aab3d0)
- Ossenkopf, V., & Henning, Th. 1994, *A&A*, 291, 943
- Palau, A., Ballesteros-Paredes, J., Vázquez-Semadeni, E., et al. 2015, *MNRAS*, 453, 3785, doi: [10.1093/mnras/stv1834](https://doi.org/10.1093/mnras/stv1834)
- Pattle, K., Ward-Thompson, D., Kirk, J. M., et al. 2015, *MNRAS*, 450, 1094, doi: [10.1093/mnras/stv376](https://doi.org/10.1093/mnras/stv376)
- Pineda, J. E., Segura-Cox, D., Caselli, P., et al. 2020, *Nature*, 4, 1158, doi: [10.1038/s41550-020-1150-z](https://doi.org/10.1038/s41550-020-1150-z)
- Pineda, J. E., Arzoumanian, D., Andre, P., et al. 2023, 534, 233, doi: [10.48550/arXiv.2205.03935](https://doi.org/10.48550/arXiv.2205.03935)
- Pokhrel, R., Myers, P. C., Dunham, M. M., et al. 2018, *ApJ*, 853, 5, doi: [10.3847/1538-4357/aaa240](https://doi.org/10.3847/1538-4357/aaa240)
- Pokhrel, R., Gutermuth, R. A., Betti, S. K., et al. 2020, *ApJ*, 896, 60, doi: [10.3847/1538-4357/ab92a2](https://doi.org/10.3847/1538-4357/ab92a2)
- Ricci, L., Testi, L., Natta, A., & Brooks, K. J. 2010a, *A&A*, 521, A66, doi: [10.1051/0004-6361/201015039](https://doi.org/10.1051/0004-6361/201015039)
- Ricci, L., Testi, L., Natta, A., et al. 2010b, *A&A*, 512, A15, doi: [10.1051/0004-6361/200913403](https://doi.org/10.1051/0004-6361/200913403)
- Rowles, J., & Froebrich, D. 2009, *MNRAS*, 395, 1640, doi: [10.1111/j.1365-2966.2009.14655.x](https://doi.org/10.1111/j.1365-2966.2009.14655.x)
- Sahu, D., Liu, S.-Y., Liu, T., et al. 2021, *ApJ*, 907, L15, doi: [10.3847/2041-8213/abd3aa](https://doi.org/10.3847/2041-8213/abd3aa)
- Sahu, D., Liu, S.-Y., Johnstone, D., et al. 2023, *ApJ*, 945, 156, doi: [10.3847/1538-4357/acbc26](https://doi.org/10.3847/1538-4357/acbc26)
- Sato, A., Takahashi, S., Ishii, S., et al. 2023, *ApJ*, 944, 92, doi: [10.3847/1538-4357/aca7c9](https://doi.org/10.3847/1538-4357/aca7c9)
- Schnee, S., Enoch, M., Johnstone, D., et al. 2010, *ApJ*, 718, 306, doi: [10.1088/0004-637X/718/1/306](https://doi.org/10.1088/0004-637X/718/1/306)
- Schnee, S., Mason, B., Di Francesco, J., et al. 2014, *MNRAS*, 444, 2303, doi: [10.1093/mnras/stu1596](https://doi.org/10.1093/mnras/stu1596)
- Shirley, Y. L., Huard, T. L., Pontoppidan, K. M., et al. 2011, *ApJ*, 728, 143, doi: [10.1088/0004-637X/728/2/143](https://doi.org/10.1088/0004-637X/728/2/143)
- Shirley, Y. L., Nordhaus, M. K., Grcevich, J. M., et al. 2005, *ApJ*, 632, 982, doi: [10.1086/431963](https://doi.org/10.1086/431963)
- Smullen, R. A., Kratter, K. M., Offner, S. S. R., Lee, A. T., & Chen, H. H.-H. 2020, *MNRAS*, 497, 4517, doi: [10.1093/mnras/staa2253](https://doi.org/10.1093/mnras/staa2253)
- Spezzi, L., Petr-Gotzens, M. G., Alcalá, J. M., et al. 2015, *A&A*, 581, A140, doi: [10.1051/0004-6361/201425417](https://doi.org/10.1051/0004-6361/201425417)
- Stutz, A. M., Tobin, J. J., Stanke, T., et al. 2013, *ApJ*, 767, 36, doi: [10.1088/0004-637X/767/1/36](https://doi.org/10.1088/0004-637X/767/1/36)
- Stutzki, J., & Guesten, R. 1990, *ApJ*, 356, 513, doi: [10.1086/168859](https://doi.org/10.1086/168859)
- Testi, L., Birnstiel, T., Ricci, L., et al. 2014, *Dust Evolution in Protoplanetary Disks* (eprint: arXiv:1402.1354), 339–361, doi: [10.2458/azu_uapress.9780816531240-ch015](https://doi.org/10.2458/azu_uapress.9780816531240-ch015)
- The CASA Team, Bean, B., Bhatnagar, S., et al. 2022, *PASP*, 134, 114501, doi: [10.1088/1538-3873/ac9642](https://doi.org/10.1088/1538-3873/ac9642)
- Tobin, J. J., Hartmann, L., Looney, L. W., & Chiang, H.-F. 2010, *ApJ*, 712, 1010, doi: [10.1088/0004-637X/712/2/1010](https://doi.org/10.1088/0004-637X/712/2/1010)
- Tobin, J. J., Chandler, C. J., Wilner, D. J., et al. 2013, *ApJ*, 779, 93, doi: [10.1088/0004-637X/779/2/93](https://doi.org/10.1088/0004-637X/779/2/93)
- Tobin, J. J., Looney, L. W., Li, Z.-Y., et al. 2016, *ApJ*, 818, 73, doi: [10.3847/0004-637X/818/1/73](https://doi.org/10.3847/0004-637X/818/1/73)
- Tobin, J. J., Sheehan, P. D., Megeath, S. T., et al. 2020, *ApJ*, 890, 130, doi: [10.3847/1538-4357/ab6f64](https://doi.org/10.3847/1538-4357/ab6f64)
- Tokuda, K., Fukaya, N., Tachihara, K., et al. 2023, *ApJL*, 956, L16, doi: [10.3847/2041-8213/acfca9](https://doi.org/10.3847/2041-8213/acfca9)
- Tokuda, K., Fujishiro, K., Tachihara, K., et al. 2020, *ApJ*, 899, 10, doi: [10.3847/1538-4357/ab9ca7](https://doi.org/10.3847/1538-4357/ab9ca7)
- Tsitali, A. E., Belloche, A., Commerçon, B., & Menten, K. M. 2013, *A&A*, 557, A98, doi: [10.1051/0004-6361/201321204](https://doi.org/10.1051/0004-6361/201321204)

- Tsitili, A. E., Belloche, A., Garrod, R. T., Parise, B., & Menten, K. M. 2015, *A&A*, 575, A27, doi: [10.1051/0004-6361/201322955](https://doi.org/10.1051/0004-6361/201322955)
- Valdivia-Mena, M. T., Pineda, J. E., Segura-Cox, D. M., et al. 2023, *A&A*, 677, A92, doi: [10.1051/0004-6361/202346357](https://doi.org/10.1051/0004-6361/202346357)
- Ward-Thompson, D., Scott, P. F., Hills, R. E., & Andre, P. 1994, *MNRAS*, 268, 276, doi: [10.1093/mnras/268.1.276](https://doi.org/10.1093/mnras/268.1.276)
- Ward-Thompson, D., Di Francesco, J., Hatchell, J., et al. 2007, *PASP*, 119, 855, doi: [10.1086/521277](https://doi.org/10.1086/521277)
- Wenger, M., Ochsenbein, F., Egret, D., et al. 2000, *A&AS*, 143, 9, doi: [10.1051/aas:2000332](https://doi.org/10.1051/aas:2000332)
- Williams, J. P., de Geus, E. J., & Blitz, L. 1994, *ApJ*, 428, 693, doi: [10.1086/174279](https://doi.org/10.1086/174279)
- Wilson, B. A., Dame, T. M., Mashedier, M. R. W., & Thaddeus, P. 2005, *A&A*, 430, 523, doi: [10.1051/0004-6361:20035943](https://doi.org/10.1051/0004-6361:20035943)
- Zamora-Avilés, M., & Vázquez-Semadeni, E. 2014, *ApJ*, 793, 84, doi: [10.1088/0004-637X/793/2/84](https://doi.org/10.1088/0004-637X/793/2/84)
- Zucker, C., Speagle, J. S., Schlafly, E. F., et al. 2019, *ApJ*, 879, 125, doi: [10.3847/1538-4357/ab2388](https://doi.org/10.3847/1538-4357/ab2388)